Machine Learning Insights into the Geochemical Life Cycle of the Columbia River Flood Basalts

Rachel Hampton[1,2] and Leif Karlstrom[1]

[1]*University of Oregon, Department of Earth Sciences, Eugene, OR 97403*

[2]*Kobold Metals, 64 Shattuck Square UNIT 210, Berkeley, CA 94704*

*Corresponding author: rachelhampton1120@gmail.com

ABSTRACT

Flood basalts are challenging to characterize in detail, despite enormous their erupted volumes, due to their age and chemical homogeneity. Here we explore machine learning (ML) approaches for classification and pattern identification in whole rock geochemical data of the Columbia River Flood Basalts (CRFB), which provide key constraints on magma generation, transport, and emplacement. We utilize supervised and unsupervised ML workflows to (1) classify unknown samples into an assumed CRFB stratigraphy, and (2) identify geochemical patterns independent of eruptive order that fingerprint the underlying petrologic processes associated with magma genesis and ascent. We synthesize a large new database of chemical analyses and use a high dimensional approach that leverages all possible ratios of major and trace elements. The supervised model demonstrates ~99% effectiveness for classification into Formation level classes and ~89% effectiveness on a member level from a complete labeled dataset, and slightly lower (~90%) Formation-level accuracy for a partially labeled dataset. Unsupervised clustering suggests similarities between member classes across stratigraphic boundaries in mantle source composition and crustal processing pathways. In particular, we find compositional clusters that point to a rapid expansion of crustal storage within the Grande Ronde, and primitive samples spanning all Formations that likely fingerprint persistent recharge from multiple mantle sources. Comparison of supervised and unsupervised approaches re-enforces known patterns in CRFB chemistry but also highlights areas where further data assimilation could lead to robust insights. This approach represents a powerful framework for classification and highlights significant future opportunities to objectively characterize petrologic datasets like the CRFB.

1. INTRODUCTION

Flood basalts are an exceptional endmember of mafic volcanism in both their volume and emplacement rate (Wignall, 2001; Bryan and Ferrari, 2013; Bond and Wignall, 2014; Ernst, 2014; Black et al., 2021). Physical mapping, paleomagnetic characterization, and geochemical data have long formed a basis for understanding the stratigraphy and interpreting the magmatic processes driving the Large Igneous Provinces (LIPs) associated with flood basalt eruptions (Ernst, 2014). In particular, whole rock geochemistry plus isotopic data and mineralogic data where available provide insights into the structure of crustal magma transport and chemical evolution of magmas from mantle melting to surface eruption (Bryan and Ferrari, 2013; Ernst, 2014). However, geochemical variations in LIPs, particularly with respect to crustal magma transport processes, are notoriously challenging to identify. Although flood basalts are generally chemically homogenous and often crystal poor (Marsh, 1987; Pearce et al., 2021), variation is commonly observed between different eruptive packages. But crustal processing of ascending magma often maps in a complicated way to the observed erupted stratigraphy even for smaller volume modern eruptions (e.g., Lerner et al., 2021) and compositional heterogeneity within single mappable flow units within LIPs have also been recognized (e.g., (Vye-Brown et al., 2019). Defining stratigraphy at a level granular enough to constrain variations in eruption rate through time in massive flood basalt provinces is therefore challenging (Pearce et al., 1984, 2021; Ernst and Buchan, 1997; Camp, 2013; Hastie et al., 2014; Wang et al., 2016; Karlstrom et al., 2019; Biasi and Karlstrom, 2021). Yet such cryptic fingerprints of petrologic evolution represent our best available tools for understanding the processes driving LIP eruption cycles, volatile fluxing and associated climate impacts, and ultimately the geodynamic origins of LIPs.

Large geochemical datasets collected to understand LIPs (eg. Ernst, 2014; Pearce et al., 2021), along with datasets available for basaltic systems globally (e.g., Ueki et al., 2018), represent an opportunity to test automated tools for pattern recognition and classification in a petrologic setting. In this work we build a machine learning (ML) framework that utilizes both supervised and unsupervised techniques to examine extrusive lava flow data from the Columbia River Flood Basalts (CRFB) with the ultimate goal of building a model that can (1) classify unknown samples in an assumed known stratigraphy, and (2) identify geochemical patterns independent of eruptive order that fingerprint the underlying petrologic processes associated with magma ascent. To accomplish this, we develop a workflow for manipulating the feature space

associated with major and trace element compositions to identify characteristic patterns between elements that lead to robust classification, dimensionality reduction, and clustering.

We focus on the CRFB as the youngest, best-preserved, and most comprehensively characterized flood basalt province globally (Hooper, 2000; Wolff et al., 2008; Reidel et al., 2013; Camp et al., 2017b) to demonstrate the utility of ML on large geochemical datasets. The progression of eruptive volumes and tempo defines a rapid waxing, a voluminous "main phase" defined by massive groups of flows, and prolonged waning characteristic of the LIP life cycle globally (Black et al., 2021).

Erupted lavas have been categorized at the Formation and member level (informal at this stage, so will be labeled with lower case), and even sub-member 'unit' level, on the basis of geochemistry, mapped location, and magnetic polarity (Wright et al., 1973; Mcdougall, 1976; Swanson et al., 1979; Reidel, 1982; Hooper, 2000; Barry et al., 2013; Conrey et al., 2013; Reidel et al., 2013; Reidel and Tolan, 2013; Reidel, 2015; Kasbohm and Schoene, 2018; Moore et al., 2018; Cahoon, 2020; Cahoon et al., 2020, 2023). CRFB Formations are well-recognized, however some member and finer classifications are still debated as mapping and characterization of deposits continues (e.g., Webb et al., 2019). The classification debate in part motivates our ML model development.

We have assembled a large database of published and unpublished CRFB whole rock geochemistry to train our model. These chemical analyses, while all in the modern instrumental era, span several decades of sample collection and multiple analytical facilities, therefore a primary initial challenge is to derive a common set of chemical elements to work with and a common set of labels to establish a training dataset. Applying a Supervised Classification ML analysis to this compiled database, we demonstrate ~99% effectiveness for supervised classification of unknown major and trace element analyses on a Formation level and ~89% effectiveness on a member level, based on established metrics for model precision and recall of our training data. Supervised learning approaches thus align in the identification of geochemical variations between Formations and members and generally confirm the robustness and utility of member-level stratigraphy in the CRFB, although we also identify consistent signatures of stratigraphic ambiguity that lead to non-unique classifications in some cases. We apply the

classifier as an application to a suite of samples (N=1,561) that did not have member-level labels in our database as an additional independent test.

We then use unsupervised learning methods to demonstrate that, while Formation-level differences are largely identifiable algorithmically, members are blurred when stratigraphic position and polarity is not assumed. In particular, unsupervised clustering suggests a far smaller number of categories is required to explain the chemical variation within the CRFB. We interpret these clusters as reflecting variations in mantle source composition and Recharge-Assimilation-Fractional Crystallization (RAFC) processes within the crust ('path effects', borrowing terminology from seismology). Some clusters suggest systematic evolution of both source and path over time in the CRFB, while others span multiple members as well as Formations and indicate recurring petrologic processes.

1.1 The Columbia River Flood Basalts whole rock geochemical database

The CRFB erupted ~210,000 km^3 of basalt onto eastern Oregon, Washington, and parts of Nevada and Idaho, with numerous long-traveling lava flows extending from the inland Columbia Basin to the ocean, hundreds of kilometers away (Wells et al., 2009; Reidel et al., 2013). Although CRFB eruptions span ~11 Myr, increasingly precise geochronology now shows that the "main phase", consisting of the Imnaha and Grande Ronde Formations was erupted between ~16.8-15.9 Ma, with the Grande Ronde Formation representing 72% of the total erupted volume was emplaced in ~450 kyr (Kasbohm and Schoene, 2018; Kasbohm et al., 2023). The CFRB onset with the Steens Formation, while post-main phase eruptions associated with the Wanapum and Saddle Mountains formations occurred with more temporal irregularity over ~10 Myr following the main phase (Barry et al., 2013; Moore et al., 2018; Kasbohm et al., 2023). A sixth formation, the Picture Gorge basalt, erupted around the same time as the Grande Ronde and perhaps earlier, possibly coeval with Steens Formation lavas (Cahoon, 2020; Cahoon et al., 2020, 2023; Pivarunas et al., 2025).

Early research on the CRFB stratigraphy (Waters, 1961; Snavely, 1962; Trimble, 1963; Gibson, 1969; Wright et al., 1973; Swanson et al., 1979) categorized flows based on field relations and petrographic evidence (e.g., the presence or absence of olivine and plagioclase) (Waters, 1961). Using these methods, the stratigraphy was classified into two large groupings and further subdivided into the Yakima Basalt group (Wright et al., 1973; Mcdougall, 1976;

Reidel, 1982; Reidel and Tolan, 1989; Swanson et al., 1989). Based on field observations it was difficult to correlate flows over the vast distances that they cover and also difficult to distinguish units with very similar petrographic characteristics (i.e. aphyric units). Low-cost XRF (X-Ray Fluorescence) technology, aided by paleomagnetic data, increased the precision of chemical correlations between flows and subdivision of the stratigraphy (e.g. Audunsson & Levi, 1997; Hooper, 2000; Jarboe et al., 2010; Wilson & Watkins, 1967). This data permitted geochemical analyses to be compiled into paleomagnetic time frame (Dominguez and Van der Voo, 2014). More recent work has sought to refine discrepancies between paleomagnetic and geochronologic timelines (Barry et al., 2013; Kasbohm and Schoene, 2018; Kasbohm et al., 2023) and isotopic characterization (e.g., Camp et al., 2013; Hooper & Hawkesworth, 1993; Mcdougall, 1976; Moore et al., 2018; Takahahshi et al., 1998; Wolff et al., 2008), refining stratigraphic boundaries using combined paleomagnetic, geochemical and field evidence (e.g., Cahoon et al., 2020, 2023; Davis et al., 2017; Webb et al., 2019; R. E. Wells et al., 2020).

Each of the six major Formations (a small seventh Formation, the Prineville Basalt (Hooper and Hawkesworth, 1993; Reidel et al., 2016), is not considered in this work) has been subsequently broken down into members and individual flows (Reidel and Tolan, 1989; Hooper, 2000; Reidel et al., 2013). Although many of these are not formal, the stratigraphy of Reidel et al., 2013 represents the most comprehensive attempt to order the CRFB at a sub-Formation level to date. Still, some member-level stratigraphic boundaries are not entirely clear-cut, either on the basis of field evidence for intermingling (e.g., Davis et al., 2017; Katona et al., 2021; Reidel, 2005) and inconsistent stratigraphic ordering (e.g., Cahoon et al., 2020; Swanson et al., 1979; Webb et al., 2019) or non-unique chemical proxies that may reflect mass loss from hydrothermal alteration (Sawlan, 2017, 2019).

Major and trace element discrimination remains a primary tool for distinguishing lavas from each other and form the basis for understanding petrologic processes. Traditionally, patterns and classification are inferred via visual inspection of geochemical biplots, in which pairs of elements or ratios of elements are plotted and assessed in terms of end member models (White, 2013). But in the absence of phenocryst populations and with bulk rock compositions that exhibit overall homogeneity, constraining flow stratigraphy can be difficult based only on binary classification of geochemical data. Reidel (2002) identified elements most useful for

bivariate classification including TiO_2, MgO, P_2O_5, and Zr, and suggested that trace elements, particularly Ba and Cr, are also useful.

Clearly it would be useful to leverage all elements together simultaneously. Previous Discriminant analysis on the Grande Ronde member level chemistry, using scores based on combinations of linear predictor variables in the geochemical data (Reidel, 1982), suggested that clustering analysis only leads to a 66% reproducibility. We aim to revisit this result here, by building a large database of modern analyses and testing different ML procedures for classification.

Our CRFB geochemical database (Supplementary Dataset S1) synthesizes 55 sources spanning nearly 40 years from the refereed and gray literature, described in Supplementary Information section S1. We do not require that samples be categorized at the member level. Because not all studies report analyses for the same elements, we consider three subsets of our data that isolate the role of major versus trace elements. These are summarized in Fig. 1. Because we focus on maximizing the number of samples N, largely focus on the member-level stratigraphy defined by Reidel et al., (2013), and include several older compilations from XRF analyses (as opposed to more complete ICPMS), none of our three datasets contain the full range of trace elements.

We take data "as is" and do not attempt to clean published datasets or correct for different reported iron oxidation states – we simply remove iron altogether from our analyses. We do not require that samples are classified at member level, which excludes 1,561 analyses from each subset (Supplementary Dataset S2). As a result, while in total our fully labeled dataset compiles N=7,975 analyses, even our least restrictive data subset D1 (major elements only: SiO_2, TiO_2, MgO, Al_2O_3, Na_2O, CaO, MnO, K_2O, P_2O_5) contains several hundred samples that are unused. Our more restrictive datasets include two subsets with different numbers of trace elements. Data subset D2 (majors + Ni, Cr, Sc, V, Ba, Rb, Sr, Zr, Y, Nb, Cu) chooses the maximum number of elements and still retains at least 7 samples in every assumed member category. Data subset D3 includes all elements in D2 plus Pb, La, Ce, and Th, representing a larger number of elements but for which not all member categories are covered. In what follows we largely focus on results from data subset D2 but include select results from D1 and D3. Our trained classification model

for these subsets can be found (along with a python Jupyter notebook for plotting) in the Supplement.

2. METHODS AND DATA ANALYSIS WORKFLOW

To characterize the variation and groupings in the CRFB geochemical database, and ultimately to interpret the processes that may have caused such variation, we require a suite of techniques that leverage the size and high dimensional nature of our dataset. We begin with a discussion of preprocessing (Section 2.1) and perform a general analysis of the CRFB dataset structure (Section 2.2) to facilitate ML algorithm selection. We then perform a Principal Component Analysis of the dataset as a preamble to high-dimensional characterization (Section 2.3) and finally describe our procedure for supervised (Multinomial Logistic Regression, Section 2.4) and unsupervised (Gaussian Mixture Model, Section 2.5) machine learning on the data.

A central challenge in applying ML methods to geochemistry is data density (Petrelli and Perugini, 2016). Several thousand analyses is not "big data", as social networks or advertising databases can comprise billions of instances or samples (Norinder and Norinder, 2022), and in Earth Science similar sized data can be found in the domains of seismology or climate science (Madhukar, 2019; Azari et al., 2021; Arrowsmith et al., 2022). The size of our database (our max in data subset D1 is 6,259 samples) is smaller in magnitude than the largest geochemical databases currently available (e.g., the global whole rock database of (Gard et al., 2019) or the GeoRoc or PETDB databases which have tens of thousands of samples or more depending on the compilation, or the Holocene volcanic rock database of (Oggier et al., 2023) has >100,000 samples), but is still large for a single volcanic province.

Our database is of sufficient size to robustly characterize high dimensional patterns with statistical confidence. Each dimension, also called a "feature" with respect to the ML algorithm, represents a geochemical feature such as element, isotope, or ratio. While the analysis of high dimensional compositional data has been considered in petrology for ~100 years (e.g., (Clarke, 1920), research on the use of automated techniques for this kind of analysis has only gained popularity within the last two decades. We will explicitly leverage the capability to analyze high dimensional data not only by simultaneously considering 9-25 elements (with a minimum of 7 analysis per dimension) but also include the ratios of elements as additional features.

2.1 Preprocessing

Before we can implement clustering and classification, preprocessing of the data is necessary to remove the influence of different units (i.e. wt.% vs ppm) and of the varying magnitudes of variation within the features. Data can be transformed or preprocessed in a variety of ways, all generally seeking to enhance variation agnostic of the original units (Aitchison, 1983; Aitchison et al., 1993; Dangeti, 2017; Geron, 2017). Preprocessing plays a major role in implementation of ML algorithms in most complex datasets. For both unsupervised and supervised ML approaches, we tested over 50 different combinations of preprocessing steps, experimenting with outlier removal, categorical balancing, and normalization. We settled on two relatively simply approaches:

Ratio Combinatorics

Geochemists regularly create ratios during bivariate analysis of geochemical data to make patterns and groupings in the data more obvious by exaggerating variation. This approach, in combination with normalization, has been shown to aid in ML classification (e.g., (Lubbers et al., 2023) (although in a linear model ratios have been shown to be of negligible use; (Aitchison et al., 1993)). The number of ratio combinations Φ between two lists is:

$$\Phi = n!\,(n-r)! \tag{1}$$

where n is the number of features (elements) in the original dataset and r is the number of features in each combination (two in this case since we are creating pairs) (Peck et al., 2005). In general, geochemical data often is expressed in terms of elemental sums (for example total alkali versus silica plots), but we limit the statistical exploration to monomial combinations here. These features reflect all possible ratios of each element, greatly expanding our data subsets from 9 major and 11-16 trace elements to a feature set of 210 (for data subset D2) or 325 (for D3). However, ratios computed according to equation (2) may have wildly different magnitudes, so we must normalize the data to compare variation equally.

Box-Cox Power Transform

We use the Box-Cox Power Transform, a nonlinear normalization that is useful for comparing non-negative distributions and making them more Gaussian in shape (Box and Cox, 1964; Howarth and Earle, 1979; Ueki et al., 2018), defined for a data vector y as

$$y^{PT} = \begin{cases} \frac{y^{\lambda}-1}{\lambda}, & if\ \lambda \neq 0 \\ \ln y, & if\ \lambda = 0 \end{cases} \tag{2}$$

where λ is a parameter found through maximum likelihood optimization (accomplished through the Sci-Kit Learn library in Python) to find the new vector y^{PT}. The transformation in equation (3) is invertible, and we generally transform back to physical units after a ML computation to facilitate interpretation.

A note on balanced classes

One of the primary challenges identified when clustering geochemical data is the lack of even sampling amongst different categories (e.g., Formation, member). This is likely due to constraints on sampling in the field, exposure biases, and differential interest in some geologic units over others (Petrelli and Perugini, 2016). There are many ways of dealing with category imbalance. The most straightforward method is just to gather more data; however, this can be costly and inefficient or even impossible in some geologic scenarios.

Oversampling or under sampling is another possibility that has seen application in some volcanologic studies (e.g. (Pitcher and Kent, 2019; Sheldrake et al., 2020)). When oversampling the number of samples in each class matches the largest sample count in any category, while under sampling the number of samples is selected based on the smallest group count. However, in a category with few samples, oversampling may have the effect of eliminating important variation. In under-sampling, categories are defined based on just a few samples which may oversimplify the variation in the dataset. In our application we see both options as unappealing and find through experimentation on synthetic data that balancing categories in the CRFB dataset causes over-fitting within the supervised and unsupervised models. While the overall accuracy on test data split from the training data goes up, model performance on unknown samples decreases dramatically. We therefore do not balance categories in this work, but do try to ensure that we have a minimum number of samples in each of the 46 assumed members to reasonably

represent their variability: the smallest sample number per member in dataset D2 (representing all given members with the largest number of elements) is 7.

2.2 Structural characteristics of the dataset

The underlying statistical structure of the dataset informs which ML classification algorithms will be most effective, what we can expect from the outcomes, and how to think about normalizing or processing the data prior to analysis. We find it useful to examine the element-wise moments of the CRFB data, as these provide clear links to standard distributions (e.g., Gaussian) that form the basis for some ML algorithms. If $f(x)$ is the probability distribution function of an element in a dataset with x the concentration, the m moments of $f(x)$ around a mean concentration c are (e.g., (Peck et al., 2005)

$$\mu_m = \int_{-\infty}^{\infty} (x-c)^m f(x) dx \quad (3)$$

Often the first few moments of a distribution are sufficient to distinguish its characteristics. The first moment μ_1 is the mean concentration (zero for central moment), the second moment μ_2 is the variance or dispersion, μ_3 is the skewness (symmetry of the distribution about the mean; -1 to 1 is considered close to a "normal" distribution) and μ_4 is the kurtosis (the 'peakiness' of the distribution; -3 to 3 is considered "normal") (Field, 2013). These moments can change with normalization or standardization as shown in Fig. 2, where the Box-Cox power transform, performed on the Grand Ronde data subset, shows not only a reduction in outliers but also the normalization of magnitudes on both axes as the distributions are centered around 0. This is a critical part of preprocessing prior to machine learning analyses, and moments provide some intuition for the clusterability of the dataset. Datasets with minimal variability (i.e. overlap between samples and between groupings) are more difficult to cluster than datasets with an increase in variability and in the separation between cluster. Too much variability results in more overlap and a decrease in the ability for the algorithm to recognize clusters.

We illustrate these trade-offs in the context of the CRFB dataset specifically by generating synthetic data with known structure. We created 10,000 synthetic test datasets with 3 centers, 10 features, 100 samples per distribution, and a range in standard deviations of the clusters from 0.1 to 7 utilizing the MakeBlobs tool in Sci-Kit Learn. We then clustered the data and related the V-score to the various data structure factors to assess the effect of different data

structures on clusterability. The V-score (called the HCV metric in Sci-Kit Learn syntax) uses ground truth labels and combines measures of homogeneity (each cluster only has samples from a single class) and completeness (all samples that have the same label are clustered together in a category) by taking the harmonic mean of the two measures (Rosenberg and Hirschberg, 2007). In order to get a perfect clustering configuration both the homogeneity and completeness must be maximized suggesting that all samples are categorized where we expect them to be (Rosenberg and Hirschberg, 2007; Geron, 2017). We utilize this to create both a synthetic regime diagram as well as for assessment of our supervised ML algorithm.

Fig. 3 shows results of this synthetic testing, plotting V-score as a function of mean pairwise distance between all points in a distribution and dip-test p-value, which is the probability that we can reject a null hypothesis that our distribution is unimodal. This regime diagram shows how clusterability varies with the structure of the underlying dataset. Lower p-values suggest more multimodal data distributions while lower pairwise distances suggest increased density of points; thus, the most highly clusterable datasets have dense, multimodal distributions.

We can then compare the synthetic data to our real data in the CRFB to assess Formation level and member level data structure and thus the applicability of various ML methods. It is well known that CRFB stratigraphic classes exhibit systematic variation along some elemental features (or ratios of elements) but are tightly clustered in others (e.g., Hooper 2007; Camp et al, 2017). For example, from Fig. 3 we can see that the Steens distribution of samples is likely close to unimodal with a dense clustering of points (also on display in the Lower Steens and Upper Steens members which themselves are nearly unimodal). Meanwhile, the Grand Ronde, Wanapum, Picture Gorge, and Saddle Mountains formations all appear very likely multimodal (this does not tell us how many groups are present, just the probability that it isn't unimodal), but have variations in the density of points with Saddle Mountains and Picture Gorge have considerably more spread in their distributions than the Grand Ronde and Wanapum formations. The complexities exhibited by this regime diagram illustrate the importance of using multidimensional analysis techniques and utilizing analysis of subset distributions within the dataset.

To motivate a choice of unsupervised learning algorithm, we also want to assess to what degree each dataset feature can be treated as a Gaussian. This can be done by comparing moments at a member level to moments expected for a Gaussian distribution (Peck et al., 2005). Most members in the CRFB dataset are well represented by Gaussian out to the fourth moment (Fig.4), suggesting that this is reasonably starting model for the CRFB data structure. The color bars in Fig. 4 represent a comparison of the distributions in each member to predicted Gaussian distributions. The lines within the plots on Panels A and B show the expected standard deviation for various values of the inter-quartile range based on the common scaling factor 1.4826 (Leys et al., 2013). In all panels, the color bar "Difference from Gaussian" is calculated by taking the estimated standard deviation value from the IQR and subtracting that from the actual standard deviation calculated from the distributions. In this way positive values show a spread that is larger than expected based on the IQR, while negative values indicate that the actual spread is smaller than expected. Values of the difference from Gaussian that are close to 0 indicate that the actual spread is roughly in line with the expected value if the distribution were Gaussian. Using this metric helps us to gauge, in addition to the expected Gaussian range for the skew and kurtosis, how close these distributions are to Gaussian in their shape.

While assuming most of the data represent Gaussian distributions, there is a group of ~10 members that have excess positive kurtosis values that indicate heavily tailed distributions (Fig. 4) arising from small groups of outlier samples. For example, the largest kurtosis is found in the Sentinel Bluffs Member of the CRB which has a distinct outlier group within its chemistry (Fig. 4). For this and perhaps other members, hydrothermal alteration has been suggested as a possible source of chemical variability within the lavas (Sawlan, 2017, 2019), but High Ti members of the Grande Ronde also show that chemical variability and outliers can also be tied to magmatic processes (Hooper et al., 2007; Reidel and Tolan, 2013). Regardless of the source, we find that these outliers are not systematic throughout all members and represent <0.5% of the data. For example, Kurtosis and skew plotted against the number of samples within each grouping shows no systematic pattern (Fig. 4). This indicates that there is no bias introduced by the imbalanced sample classes in our data and thus that we can effectively utilize logistic regression methods for supervised learning (Fig. 4).

2.3 Principal Component Analysis

To leverage the high dimensional nature of igneous geochemical data containing the standard major and trace element suites, we now apply appropriate statistical methods for quantifying variability between CRFB samples. We first perform Principal Component Analysis (PCA) as a reference model (Fig. 5). PCA is a matrix decomposition technique that facilitates dimensionality reduction to approximate the original data by rotating the coordinate axes to minimize variability (Aitchison, 1983; Aitchison et al., 1993; Praus, 2005; Filzmoser et al., 2009; Chen et al., 2015). PCA decomposition allows us to recognize the features that are responsible for that variation as well as providing tools to describe that variation (Praus, 2005; de Caritat and Grunsky, 2013; Pouget et al., 2014; Iwamori et al., 2017; Ueki and Iwamori, 2017; Cahoon et al., 2023). From a linear algebra perspective PCA represents a rotation of basis (set of coordinate axes) that is ordered such that the greatest variance of the data lies on the first of the new basis vectors (called the first 'principal component'), the second greatest variance on the second, and so on.

The new set of basis vectors completely describe the data, but often only a subset of principal components is necessary to approximate the dataset and assess which features are primarily responsible for the variation between sample instances in the dataset. In this way PCA functions as a dimensionality reduction technique (Aitchison, 1983; Aitchison et al., 1993). However, the linear combinations of the original data coordinates within principal components are not always interpretable (Lee and Seung, 2000; Vesselinov et al., 2018). We implement PCA by first computing the eigenvalues and eigenvectors of the data covariance matrix, then sorting the eigenvectors by decreasing eigenvalues (Iwamori et al., 2017; Ueki and Iwamori, 2017).

PCA is known to be strongly impacted by features with different magnitudes (Filzmoser et al., 2009), therefore we apply the power transform normalization as a pre-processing step. We do not compute all possible elemental ratios but rather ask whether linear combinations of elements are sufficient to explain the data. Fig. 5 shows that the first two principal components explain ~68% of the variance, and seven are required to get above 90% variance explained. Thus, PCA does reduce the data dimensionality, but not enough to be easily interpretable.

The first two principal components suggest groupings of elements that separate, to some extent, stratigraphic Formations (Fig. 5B) and whose eigenvector weights (Fig. 5C-D) suggest combinations of elements that can distinguish them. For example, the Grande Ronde stratigraphic member has variation that is defined by changes in Al_2O_3, SiO_2, Na_2O, K_2O and Sr, Rb, Ba, while the Wanapum formation appears to have more variation captured by changes in TiO_2, P_2O5, MnO, Y, and Nb. Steens, Imnaha, and Picture Gorge samples overlap but clearly reflect the negative weights associated with lower SiO_2 and higher MgO. This analysis suggests that high-dimensional classification may be successful and provides a comparison point for the other methods utilized.

2.4 Supervised Classification via Multinomial Logistic Regression

Applications of ML to classification generally fall into two categories: supervised and unsupervised learning (Geron, 2017). Our full workflow for both approaches is presented in Figure 6. To accomplish the supervised task of training and testing a model we multinomial logistic regression (MLR), an approach that has seen success in other geochemical supervised classification studies (e.g., (Ueki et al., 2018)). Many supervised learning algorithms exist; we choose MLR specifically for its simplicity, and transparency of evaluation, and efficiency. The result of an MLR classification is the probability of a categorical target variable belonging to a certain class (Fig. 1). The dependent or target variables, in the case of our CRFB application, are lithostratigraphic positions, the features of the dataset are the elemental concentrations and ratios, and the instances are individual samples.

The MLR algorithm is as follows (Peck et al., 2005; Geron, 2017; Ueki et al., 2018; Itano et al., 2020): (1) A linear model for the distribution of target classes is defined, involving a weighted sum of all features. (2) Guess the weights and predict classifications using a sigmoid function to assign a probability between 0 and 1 that a sample is part of a particular class. (3) Define a cost function using the known class labels and minimize this cost function with gradient descent algorithm to find the weights that minimize cost while maximizing the probability. We use the cross-entropy cost function, a maximum likelihood estimator of weights that maximizes probability (Pedregosa et al., 2011). (4) The model parameters are constrained once a set of weights has been found, but we then repeat with random initial starting weights (we use 50

iterations) and gradient descent calculations (1200 maximum iterations each) to find the best model.

We use a random train-test-split approach to validate the MLR model that randomly sets aside 30% of the data to be used as test data. On our dataset of full CRB samples this resulted in ~700-800 test samples, depending on the elements used. For each iteration of the training model, test data are classified, then assessed in terms of accuracy, precision and recall (Pedregosa et al., 2011). Accuracy quantifies how well the model predicted classes match with the known labels for the test data. Precision is defined as the ratio between "true positives" and the sum of "true positives" and "false positives", indicating how well correct predictions were made (Geron, 2017). Recall is defined as the ratio between "true positives" and the sum of "true positives" and "false negatives", indicating how well the model identified incorrect predictions (Geron, 2017).

Once the highest accuracy model is chosen from the 50 iterations of starting weights, we finally train a model using these parameters on the complete test dataset (not just 70%). This is the model used to predict unknown samples. For each population that is analyzed, every sample is given a suite of probabilities that provide a quantitative measure for how likely it is that a given sample fits into each class.

To visualize MLR training success and failure, we plot each sample based on the model predicted stratigraphic category vs the original labels given to the sample in the dataset, defined by (Reidel et al., 2013). This 'confusion matrix' represents the relative proportion of each known label classified into a predicted group and is normalized to show the proportion of each sample class (y-axis), that was categorized into each predicted stratigraphic label (x-axis) (Fig. 7). We focus on detailed presentations of the D2 data subset here (Fig. 1), although qualitatively similar results were found for D1 and D3 (Supplementary Table S1).

At the Formation level, the best training score on the preprocessed features resulted in an overall accuracy, recall, and precision of ~99%. This high accuracy is suggestive of a strong stratigraphic framework overall, with a few instances within the stratigraphy where members appear more closely related within the formations than is suggested by hard stratigraphic boundaries. At the member level, we have a slightly lower overall accuracy (~89% for D2) but overall find consistency with the Formation-level result as incorrect classification largely is restricted to within-Formation members (Fig. 7B). Overall uncertainty within the model appears

to be primarily related to member level categories with less data. This is a much larger factor than outliers in affecting classification probabilities as the classes with some of the strongest outlier groups are also the ones that have very high classification probabilities.

Fig. 7 provides a guide for MLR accuracy, but much more information is provided on a sample-by-sample basis, because each candidate class is assigned a probability by the MLR model prediction. We visualize this with a circular bar plot for each sample that describes the full suite of probabilities for each class, labeling probabilities >10%. Fig. 8 shows two example classifications (from the unknown dataset to be discussed subsequently). Fig. 8A shows a robust classification in which the sample is predicted to be Wapshilla Ridge with an 85% probability. Fig 8B shows a more ambiguous classification, with three possible member classes (all within the Grande Ronde) each with probabilities >25%. This more detailed look suggests that there is more ambiguity in the overall predictive power of the MLR model than is suggested solely by the high scores during model training.

An obvious question is why some samples are easier to classify than others. We address this by examining the coefficients in our trained MLR models. Coefficients in and of themselves describe which features the model uses and in what weight to make decision boundaries between the classes of interest (in this case the stratigraphic boundaries). We use this to understand what separates and differentiates the classes in a multidimensional space. The pattern of coefficient magnitudes shows that some Formations seem to be clearly classified with 1-2 coefficients (Fig. 9). For example, Grande Ronde and Steens are both distinguished on the basis of SiO_2 (more evolved and less evolved than other Formations, as evident by positive and negative coefficients in Fig. 9.B). Saddle Mountains seems dominantly distinguished on the basis of Nb/Zr, a ratio between a more immobile and incompatible element versus a more compatible element that can be used as an indicator of more primitive magmas (high Nb/Zr) versus magmas that have experienced more crustal contamination or fractionation (lower Nb/Zr). Another interesting comparison is Y/V, which ranks second for Imnaha with a positive coefficient and first for Wanapum with a negative coefficient (Fig. 9.B); Y/V also appears with negative weight for Steens. It's presence as a helpful indicator between Imnaha, Wanapum and Steens basalts could provide a useful indicator element in the future for distinguishing samples in these formations.

For Formation classes in which the MLR classification is more evenly distributed amongst 10 (or more) features, the model is leveraging the high dimensional nature of the data to create decision boundaries between classes and decide how much to rely on the decision boundary of each feature. Wanapum and Imnaha, and to some extent Picture Gorge, demonstrate this flat pattern (Fig. 9.A), where significantly more features are needed to distinguish between samples in these classes. One interesting note is that neither MgO nor CaO appear in the top 10 feature list, although these elements commonly appear on bivariate plots used to visualize the CRFB. This indicates that certain class boundaries are more definitive in other feature dimensions and perhaps more elements can be used to reliably describe the difference between stratigraphic classes.

At the member level, similar examination reveals that only a small number of members can be distinguished based on 1-2 elements, notably Upper Steens, Buckhorn Springs and Esquatzel (Fig. 10). A few others, Birch Creek, Roza, and Meyer Ridge, also have a relatively steep pattern of MLR coefficients, indicating that fewer features are required by the model to separate those classes, making them more chemically distinct from other members in the stratigraphy. Most other members require more multidimensional weight to be placed on the decision boundary analysis for classification.

2.5 Unsupervised Clustering using a Gaussian Mixture Model

The supervised classification problem specifies categories, but for the CRFB there remains debate at a sub-Formation level about stratigraphic boundaries. We also want to understand the petrologic pathways reflected in observed lava compositions. These are both problems where we can leverage the strengths of unsupervised learning, defined by a set of algorithms that seek to separate a dataset into categories. Unsupervised learning is often associated with dimensionality reduction or blind source separation (Carniel and Guzman, 2012; Petrelli and Perugini, 2016; Geron, 2017), assuming no prior information on categories such that groupings may cross stratigraphic boundaries. These methods are now ubiquitous in seismic applications (e.g., (Holtzman et al., 2018))and are becoming common for classification problems across volcano science (e.g., (Boschetty et al., 2022; Kubo Hutchison et al., 2023; Jutzeler et al., 2024)).

A generic workflow for unsupervised ML involves preprocessing the data, determining the correct number of components or clusters, assessing the outcome and repeating until the best fit model parameters can be found, and finally interpreting the output. There are dozens of known clustering algorithms, but not all perform well on non-negative geochemical data (Lacassie et al., 2006; Templ et al., 2008; Pedregosa et al., 2011; Iwamori et al., 2017; Ueki and Iwamori, 2017). For example, the k-means algorithm is excellent at choosing isotropic clusters, but fails to predict cluster boundaries for complex data distributions (Pedregosa et al., 2011; Ellefsen et al., 2014; Geron, 2017). Other methods, such as DBSCAN, are excellent for noisy datasets but are very dependent on user-defined parameters and can thus be non-unique (Pedregosa et al., 2011; Geron, 2017).

We implement the Gaussian Mixture Model (GMM) algorithm which assumes the data is well described by a multivariate Gaussian distribution (Pedregosa et al., 2011; Ellefsen et al., 2014). This algorithm generalizes k-means to include covariance between each data dimension, implemented as GaussianMixture in Python's Sci-Kit Learn library (we use the covariance_type="full" option). GMMs take a probabilistic approach to drawing high-dimensional cluster boundaries, and each sample is assigned a probability for each class. The number of desired clusters (or "components") must be specified for the dataset at the outset; this becomes a primary parameter in the GMM model fitting exercise. The model begins by randomly seeding the cluster components and calculating the probability that each sample was generated by each of those components (Pedregosa et al., 2011; Geron, 2017). This 'expectation maximization' process is repeated until the highest probability can be found across all the samples (Dempster et al., 1976).

Measuring success

Measuring the success of unsupervised learning can be very difficult when there are no ground truth labels for the categories. To assess the best number of clusters we use two metrics to assess how well a given number of clusters fits the data. The BIC (Bayesian Information Criterion) and AIC (Akaike Information Criterion) metrics both favor the most efficient model that maximizes the probability that each sample belongs to a given class (i.e. The lowest AIC and BIC scores) while also penalizing for excessive model parameters (Hastie et al., 2001) to assess overfitting.

If AIC and BIC do not reach a clear minima, cluster number is often determined by slope breaks in the AIC/BIC score as a function of cluster number (the 'elbow test') (Hastie et al., 2001). We will find that this is an issue for the CRFB dataset. Rather than seek a unique number of clusters for our GMM model, we take a more exploratory approach and assess the sensitivity of cluster properties to their number (as well as to the database subset used). We can also assess the success of clustering by computing the V-score metric introduced in Section 3.1 as well as the 'Silhouette Score' (Hastie et al., 2001; Rosenberg and Hirschberg, 2007; Pedregosa et al., 2011; Geron, 2017), which measures how overlapping clusters are. Silhouette scores closer to 1 indicate better clustering, while negative values indicate mis-clustering.

3. PREDICTING CRFB STRATIGRAPHIC LABELS USING SUPERVISED CLASSIFICATION

As an application of our MLR classifier, we predict the stratigraphic labels for a subset of our CRFB dataset, from numerous published sources, as "undifferentiated" with Formation but not member label provided. This dataset (Supplementary Dataset S2) comprises 1,561 samples that span the elements in our data subset D2, which we will exclusively use as the ML classifier here so as to include all assumed members with the largest number of features. The unknown data spans all Formations except Picture Gorge, and because the Formation labels are given, we can test the accuracy of our model at this level. This provides an independent assessment of model robustness, which we can then use in the context of the predicted member labels for which we have no ground truth.

Fig. 11 shows the results of our prediction (probabilities of Formation and member level categories for every sample are included in Supplementary Data File S2). We predict a classification of 1,346 samples at greater than 0.75 probability at Formation, 86% of the unknown dataset. Somewhat unexpectedly, we also find that considering the highest probability classification for each sample results in only an 89% success rate in matching the given Formation labels (in other words, we predict the wrong label for 11% of the dataset). While still a high success rate, 89% is lower than the 98% accuracy predicted by the train-test-split approach described in Section 3. Of the misclassified samples, 173 samples have two separate probabilities >0.25 and 42 have a single classification below 0.75. There are three possible explanations: (1) the precision/recall/accuracy metrics are not a sufficient characterization of

MLR model training, (2) some samples represent outliers not captured by the model training dataset, or (3) some of the labels (either in the training data or the unknown data) are incorrect. We do not attempt to assess (3) here or fully explore (1). However (2) is plausible; for example, samples labeled as Picture Gorge were not a part of the unknown dataset but were predicted at >0.9 probability for 19 samples. Picture Gorge is known to share similarities with primitive samples in other Formations (Wright et al., 1973; Wolff and Ramos, 2013; Cahoon, 2020; Cahoon et al., 2020, 2023) but is under-represented in our training dataset compared to the others.

We generally find increased accuracy of predictions by setting a threshold probability. For example, if we restrict only to samples with a classification probability of 0.9 or more, we still classify 1136 samples at Formation level but correctly predict the label for 92% of these. This suggests that applications of the MLR classifier to unknown samples should consider only samples with high probability of classification.

When we apply our classifier at the member level, we find that the total number of samples predicted with >0.75 reduces somewhat to 893 samples (57% of the unknown dataset). At this more granular level, we also see a larger proportion of samples classified multiply at lower (but still significant) probabilities (e.g., Fig. 8B). Of these, 334 samples have two members that are predicted at more than 0.25 probability, while 668 in total have a maximum classification probability below 0.75. Fig. 12.A-B shows the distribution of predicted members in the unknown dataset at greater than 0.75 probability and less than 0.25 probability.

It is interesting to examine the samples for which the MLR model struggles to find a clear category. These samples shed light on similarities between categories that likely reflect the underlying petrologic processes that challenge MLR classification. Fig. 12.B shows the distribution of low probability classifications across members, and Fig 12.C shows the pair-wise distribution. We see that there is a tendency to multiply classify within Formations, and between stratigraphically adjacent Formations. In particular, samples in the Grande Ronde and specifically the Wapshilla Ridge and Sentinel Bluffs members pose a challenge for the model. These members have the highest sample number representation in the training dataset (Fig. 1), so we cannot explain this ambiguity by lack of training data. A more plausible explanation is that these members exhibit real variation and commonalities with the chemistry of other members.

Finally, although we have emphasized where the model fails in this discussion, Fig. 12 also illustrates notable successes: for some members we see very little ambiguity in MLR classification. Asotin, Priest Rapids, Meyer Ridge, Kendrick Grade, and Rock Creek all exhibit many more robust (>0.75) than ambiguous (<0.25) classifications, with few multiple classifications. This indicates that the MLR model recognizes real variability in the CRFB geochemistry and classifying appropriately. Overall, the independent assessments of MLR classification accuracy performed here (the train-test-split exercise and the classification of unknown samples with ground-truth Formation labels) suggest that our model can be used with confidence to categorize CRFB geochemical analyses into the established Formation and member level stratigraphy at >90% confidence, especially if the maximum MLR probabilities are higher than 0.9. Supplemental datasheet S2 includes our predicted Formation and member level classifications as well as the max probabilities.

4. UNSUPERVISED CLUSTERING TO ELUCIDATE COMMON PETROLOGIC PATHWAYS

The results of the supervised classification invite further investigation and exploration of the groupings within the CRFB. An obvious question is: if we applied unsupervised classification to our CRFB lava dataset, do we recover the known Formation and member level stratigraphy? In general, we do not. Instead, we find groupings of samples for which chemical composition is similar across stratigraphic boundaries. These we will suggest reflects common source (mantle melt compositions) and path (crustal processing) contributions. However, we also find that clusters can be associated in a qualitative way with stratigraphic height. This indicates an overall chemical evolution of CRFB lavas over the lifetime of the LIP.

We evaluate the optimal number of clusters based on lowest AIC and BIC scores as outlined in Section 3.5, exploring a range of clusters from 2 to 50 (encompassing the given number of Formations and members). We summarize the results in Fig. 13 for all three data subsets. The BIC minimum predicts 29 clusters for D1, 5 clusters for D2, and 3 clusters for D3. The AIC metric has no minimum for D1, predicts 25 clusters for D2, and 16 clusters for D2.

Diminishing returns are expected when increasing the number of data dimensions while only moderately increasing the dataset size (Hughes, 1968), and as before focus on interpretation

of data subset D2 (largest number of elements with at least 7 samples spanning all members in Fig. 1). A notable feature of the AIC pattern for D2 is the broad global minimum, with ~17-28 clusters exhibiting similar AIC values. This is borne out by examination of other metrics – there is variation of less than ~1% in both V-score and Silhouette scores over this range. Moreover, we find that GMM generates empty clusters for higher numbers. We choose to analyze two cases here: 5 clusters (V-score of 0.42, Silhouette score of 0.23), corresponding to the BIC minimum of D2, and 21 clusters (V-score of 0.72, Silhouette score of 0.24), a representative of the broad AIC minimum of D2. We note that the 21 cluster case exhibits one empty cluster (a feature common to GMM modeling) – we thus discuss only the 20 non-empty clusters in what follows. Assuming more clusters in GMM models generally results in more empty clusters, which indicates diminishing returns of the GMM.

The case of 5 clusters is close to the assumed number of Formations (6 in total), while the case with 20 clusters is far more than the number of Formations but less than half the assumed number of members (46 in total). We compare the distribution of samples in each GMM cluster to the corresponding Formation and member level labels. Fig. 14 and 16 show the Formation and member level comparison. On these plots, yellow boxes indicate that no samples from a given classification appear in the corresponding GMM cluster. Grayscale boxes with numbers indicate the fraction of the GMM cluster occupied by the corresponding class (columns sum to unity). Histograms show the number of samples in each GMM cluster and each class label.

It is also interesting to examine the GMM clusters in chemical biplots, to seek patterns that might be interpretable petrologically. We invert our Power-Transformed data back to real units (e.g., Fig. 2; Supplement Figs S4-S5), and plot according to elements or ratios that either have been used in other CRFB studies or that were found to be important for MLR supervised classification. The fitted GMM model in both cases is included as supplementary material. Fig 15,17 show these biplots; each circle is the median and error bars are the interquartile range of values for a given cluster, while symbol color indicates GMM cluster number (as given on Fig. 14,16).

For the Formation comparison with 5 GMM clusters, Fig. 14 shows that Cluster 0 encompasses samples from all Formations, while Fig. 15 shows that Cluster 0 contains the most primitive samples in the dataset. We interpret this cluster to represent samples that best reflect

the mantle source(s) of the CRFB. Cluster 1 and 2 dominantly encompass samples from the Grande Ronde and Wanapum but also include a fraction of samples from the earlier phases (Steens, Imnaha, Picture Gorge). These clusters are somehow transitional, and we hypothesize are reflective of increasing AFC influence in biplots. Cluster 3 contains dominantly Grande Ronde samples and is interpreted as reflecting the unique characteristics of this Formation, although small fractions of Saddle Mountains samples also are found in this cluster. Cluster 4 is dominantly Saddle Mountains, very high in Zr and Ba (incompatible tracers that indicate more magmatic evolution and FC contributions).

Overall, while samples in GMM clusters span multiple Formations, the geochemical composition of cluster features varies in a systematic way that seems to reflect progressive crustal processing (AFC). Although not mapping one-to-one with stratigraphic order, the ordering in Fig 14 and corresponding array in Fig. 15 indicate a systematic progression of CRFB composition through time away from primitive compositions. However, primitive samples also appear in all Formations (cluster 0).

The member comparison with 20 GMM clusters is more complex but also potentially more informative about process – from here forward, when a cluster number is referenced, it is with respect to this GMM model. Once again, we see a rough correspondence with stratigraphic order in Fig. 16, and once again we see clusters that contain samples spanning multiple members. A higher V-score at this cluster number suggests that at this level the GMM is capturing more clearly distinct groups than for the five cluster example. We represent cluster median and interquartile range values in terms of biplots on Fig. 17. Here we choose element ratios in part based on those predicted from MLR to be the most important discriminants: Zr/P_2O_5, Zr/Ba, Nb/Zr, and SiO_2 are the highest magnitude coefficient in our Formation-level MLR model, and as expected these broadly separate the fields. We also plot Ni versus MgO to look for distinct mantle source compositional trends following (Soderberg and Wolff, 2023), and plot trace elements Cr versus Rb as these are sensitive to AFC with Idaho Batholith as assimilant ((Wolff and Ramos, 2013); also see Supplemental section S2) .

With the insights from Fig. 16 and 17, we find that it is possible to interpret the 20 GMM clusters. Clusters 0-4 nearly encompass the early CRFB Formations and Picture Gorge, so represent onset phases of the CRFB life cycle. With one exception, these clusters form the end of

a broad array on Ni vs MgO plot, with clusters 3 and 4 (both contain a large fraction of Picture Gorge samples) forming a distinct trend from clusters 0-2. We interpret these clusters as tracking distinct mantle sources (e.g., (Soderberg and Wolff, 2023)).

Clusters 5-11 are almost entirely composed of Grande Ronde (GRB) samples, but there are interesting sub-groupings to examine. Cluster 5 plots towards primitive influence, similar to clusters 0-4 although it is entirely composed of Grande Ronde samples. Clusters 10-11 have a small number of Picture Gorge samples. We suspect that these represent episodes of mantle recharge. Clusters 6-9 span several Grande Ronde members in entirety, although all are mainly composed of Wapshilla Ridge samples. They form a tight cluster on several of the biplots, characterized by the highest SiO2 and incompatible trace element values.

Although some Wapshilla samples appear in other clusters, the following members are entirely spanned by clusters 6-9: Center Creek, Kendrick Grade, Skeleton Creek, Downey Gulch, and Ortley. If we include cluster 11, additionally Grouse Creek, Mt Horrible, Hoskin Gulch, and China Creek are completely characterized. We note that Cluster 11 is dominantly Sentinel Bluffs samples, and along with Cluster 10 includes Picture Gorge samples suggesting a recharge influence. Cluster 6 includes Saddle Mountains samples from Wilbur Creek and could also plausibly represent influence from the process of magma recharge. Notable in the Grande Ronde clusters is that that Meyer Ridge occupies almost its own cluster (#10), while Cold Springs Gulch, Brady Gulch, and Indian Ridge share one (#5). Sentinel Bluffs spans many clusters, both those representing early/primitive influence as well as clusters residing within the Saddle Mountains.

Clusters 12-14 map onto Wanapum Formation nearly completely, but notably the Eckler Mountain member spans clusters associated with Imnaha and Picture Gorge as well as GRB (Teepee Butte) samples. Clusters 15-19 then map onto Saddle Mountains members. Umatilla is mapped 1-to1 between GMM cluster 15 and the given member; it is the only cluster to encompass all samples of a member class in Fig. 17. Cluster 16 (Asotin and Weissenfels Ridge) and 19 (Weippe and Pomona with small amount of Sentinel Bluffs) plot more in the primitive chemical fields and suggest recharge influence, while others in this group are among the most evolved. This is consistent both with previous interpretations and observations that the majority of the variation within the entire CRB is captured by the Saddle Mountains Formation and not by

the main phase (Hooper, 2000; Conrey et al., 2013; Reidel et al., 2013; Wolff and Ramos, 2013; Camp et al., 2017a).

5. DISCUSSION

The primary goals of this study are to apply a machine learning (ML) workflow to the Columbia River Flood Basalt (CRFB) lava whole rock chemistry, building models to (1) objectively classify unknown samples into established stratigraphy, and (2) identify common patterns underlying the geochemical data independent of eruptive order. To accomplish this, we conduct three classes of statistical analysis using ML tools. First, we characterize the dataset and conduct Principal Component Analysis. Then we build a Multinomial Logistic Regression model (supervised ML) and a Gaussian Mixture Model (unsupervised ML) of a large new whole rock major and trace element lava database (Supplementary Dataset S1). Together the supervised and unsupervised approaches accomplish our goals, albeit raising questions about the CRFB stratigraphy and identifying clear systematic signals of distinct petrologic pathways. The following discussion synthesizes our ML results and points to future applications of these methods.

5. 1. Implications of machine learning for the stratigraphy of the CRFB lavas

Decades-long efforts underly the mapping and categorization of CRB lavas at Formation, member, and even more granular unit stratigraphic levels (e.g., (Reidel, 1982; Reidel and Tolan, 1989; Hooper, 2000; Reidel et al., 2002, 2013; Camp, 2013; Camp et al., 2013; Martin et al., 2013; Moore et al., 2018; Cahoon et al., 2023). That member level classifications are still ambiguous (e.g., (Davis et al., 2017; Webb et al., 2019)) speaks to the challenges of disentangling eruptive products in such a chemically homogeneous sequence of lavas. Classification in a high dimensional system with systematic variability (as demonstrated by our initial statistical characterization of the dataset Fig. 3-4) is an area where supervised learning approaches are expected to excel, and indeed the MLR classifier is extremely successful in the majority of cases studied here. The D2 model exhibits ~89% success at recovering known member labels in our test dataset and ~99% success at the Formation level (although as discussed in Section 3, we suspect a true accuracy of ~90% based on application to an unknown dataset). The unsupervised GMM clusters recover known chemical groups such as similar

primitive signatures across Steens, Imnaha, and Picture Gorge samples, and more subtle discriminators such as the "TiO_2 gap" identified by Hooper et al., (2007) that separates Wanapum from underlying Formations (Supplementary Fig. S3.A).

But what to make of the cases where the MLR model fails? Fig. 12 shows that ambiguous classifications of our unknown dataset are not random and occur persistently with certain members, for example Buckhorn Springs (GRB) and American Bar (Imnaha), and then between Wapshilla and Sentinel Bluffs, Winter Water (both GRB), and Frenchman Springs (Wanapum). In every one of these cases, GMM clusters – a completely independent method – grouped some samples from these paired members together. GMM cluster 2 contains both Buckhorn Springs and American Bar, cluster, clusters 6-10,11 have various groupings of Wapshilla with Winter Water and Sentinel Bluffs, while cluster 13 includes Wapshilla samples along with Frenchman Springs. That both supervised and unsupervised ML classifications cross stratigraphy to group members together, suggest two possible interpretations: (1) the CRFB member stratigraphy is not as robust as we've assumed here, or (2) there are common processes occurring at multiple times within the stratigraphy. Ongoing discussion about CRFB stratigraphy in the literature suggests that (1) may be partially true, but we will focus here on the implications of (2).

The precise number of GMM clusters is not certain at this stage in our analysis (within or between database subsets), although the qualitative patterns discussed in Section 4 are robust for different choices of cluster number. We expect that additional chemical features (for example HFSRE elements sensitive to garnet (Takahahshi et al., 1998), mineral-scale constraints (Petcovic and Grunder, 2003) isotopes (Mcdougall, 1976; Dodson et al., 1997; Wolff et al., 2008)), magnetic polarity (Pivarunas et al., 2025), high precision geochronology (e.g., (Kasbohm et al., 2023)) and information about known stratigraphic position will increase the uniqueness of GMM clusters. We hope that future work along these lines can establish clusters that objectively define a member-level stratigraphy of the CRFB.

Our statistical workflow is naturally suited for identifying outliers and compositional trends that reflect a variety of processes. As illustrated in Fig. 4, members that do not follow the overall trend in these elements and plot more than three standard deviations away from average compositions predicted by Gaussian distribution, are a group of outlier compositions that in most cases are dictated by highly enriched trace elements. Although representing a small number of

samples (<0.5% of the dataset), it is possible that the variation in these samples may have been imparted during post eruption cooling and crystallization or hydrothermal alteration processes (e.g. (Sawlan, 2017)). However, outlier groups in dimensions such as Rb (a fluid mobile element sensitive to alteration) show only small population sizes (2 samples from the Imnaha formation show anomalous Rb, as do a population of undifferentiated Grande Ronde samples) and suggest that if this process is present, much of the data remains unaffected. Additional signals in elements such as V could also be indicative of changes in the redox state of the system, which was not investigated in detail during this study but presents a potential future direction of study. We expect that systematic examination of GMM cluster output identifies groupings of samples across stratigraphic boundaries that exhibit geochemical signals attributed to post-emplacement chemical differentiation in addition to crustal RAFC as considered here.

5.2 Implications for time-evolving magma storage and eruption

Our goals in this manuscript are largely methodological, but nonetheless with compositions of the different clusters identified we can relate these objective groupings to the relative timing of RAFC processes in the CRB geochemical stratigraphy. Numerous studies have applied general considerations of RAFC on whole rock chemistry (e.g., O'Hara and Mathews, 1981; Lee et al., 2014) to the CRFB (e.g., Wolf and Ramos 2013; Yu et al., 2015; Moore et al., 2018). We conduct a set of thermodynamic simulations motivated by these studies to ground similar interpretations in our CRFB data. These simulations are described in Supplement Section S2. We use the Magma Chamber Simulator, an energy-constrained phase equilibria calculator (Bohrson et al., 2014), to predict major and trace element evolution for idealized RAFC scenarios at 5 kbar pressures with an assumed Imnaha parent and different possible assimilant compositions, including the Wallowa Batholith and Idaho Batholith (Supplementary Fig. S1-S2). These simulations provide a guide for interpreting variation seen between GMM clusters (arrows on Fig. 15 and 17). They are not intended to be a complete parameter exploration, and we therefore view the resulting RAFC as semi-qualitative, setting the stage for future work that seeks to integrate petrologic constraints with thermomechanical considerations of crustal magma transport. For details of the parameters utilized see Supplement Section S2.

Considering the entire CRFB, we first examine the relationship between member labels of each chemical analysis in the database to the GMM label assigned, with 5 and 20 clusters as

comparators to Formation and member labels. At a Formation level (Fig. 14), we see that samples from the Steens, Imnaha, and Picture Gorge all group together and are found through all later Formations. This suggests that compositional signatures of primary mantle melts are found throughout the stratigraphy and suggest persistent recharge. This "primitive" cluster splits into multiple groupings that have clearer member-level comparators in the 20 cluster case (Fig. 16), which suggest different mantle sources spanning Steens, Imnaha and Picture Gorge (e.g. (Soderberg and Wolff, 2023; Cahoon et al., 2023). We also see evidence for recharge within Grande Ronde, Wanapum, and Saddle Mountains Formations via clusters that are both clearly compositionally distinct from other nearby members but also trend back towards primitive compositions (Yu et al., 2015) defined by other clusters (Fig. 15 and 17). For example, clusters 14 and 10 (dominantly Priest Rapids and Meyer Ridge, with other minor contributors) seem plausibly like RAFC products of cluster 2 (Imnaha) in Fig. 17.C-D. It is notable that recharge-signature clusters are associated with transitional members between Imnaha and Grande Ronde, and again between the Grande Ronde and Wanapum (Fig. 16).

The greatest degree of overlap between distinct members occurs in clusters associated with the Grande Ronde, and these clusters also trend towards more evolved compositions expected for assimilation of continental crust. This suggests a common tendency towards AFC with significant crustal interaction, as would be expected for residence in a common storage zone. It is tempting to use the proximity of clusters 6-9 and 11 in Fig 16-17 as evidence for a common reservoir or crustal differentiation pathway for these Grande Ronde members, involving a sudden increase in storage zones that provides expanded surface area for assimilation (e.g., (Karlstrom and Richards, 2011). Indeed, clusters 6 and 9 (early and later GRB but both containing Wapshilla Ridge samples) are offset from the arrays in Fig. 17C-D and are plausibly more clearly AFC dominated based on our petrologic models (red arrows).

Nearly coeval emplacement of some of these members (e.g., Mt Horrible, Grouse Creek, Wapshilla Ridge) has been previously suggested by interfingering of near vent deposits (Davis et al., 2017). Indeed, 'transitional contacts' between lavas are suggested for all R2 magnetic polarity section (Reidel and Tolan, 2013). It is worth noting that the span of members represented by clusters 6-9 and 11 represents a combined volume of 108,800 km^3, a staggering ~51% of the entire CRFB erupted volume and ~71% of the Grande Ronde Formation (Reidel and

Tolan, 2013; Reidel et al., 2013, 2016). Combined U-Pb and $^{40}Ar/^{39}Ar$ high precision (Kasbohm et al., 2023) puts the entire GRB emplacement duration at ~450 kyr. Individual ages obtained by Kasbohm et al., (2023) at the Ortley member and Center Creek member span all samples in clusters 6-9 and 11 and imply a shorter duration of ~240 kyr The implied average eruption rate for these members – without considering the other units in the stratigraphy that do not lie in GMM clusters 6-9 and 11 – is ~0.45 km^3/yr (noting that individual eruptions likely have exhibited instantaneous eruption rates orders of magnitude higher, (Biasi, 2021; Biasi and Karlstrom, 2021)).

However, thermomechanical considerations (e.g., (Karlstrom et al., 2012; Geshi and Neri, 2014; Mittal et al., 2021)), observational evidence (e.g., (Mittal and Richards, 2021)), and petrologic modeling (e.g., (Wolff and Ramos, 2013)) suggest at most 10-30% of total stored volume can be erupted in LIP-scale eruptions. Assuming a representative 10:1 intrusive: extrusive ratio this implies that a central storage zone for these members processed volumes in excess of 10^6 km^3, and when combined with eruptive age constraints the implied magma flux is on the order of 4 km^3/yr. This is similar order of magnitude although larger than the 'primary magmatic flux' estimated based on petrologic modeling to explain the assimilation signature of the GRB by Wolff and Ramos (2013).

And yet, the Grande Ronde itself cannot be fully explained by a single reservoir or differentiation pathway – the distinct clusters seem to imply multiple storage zones, with different RAFC histories. These clusters are comprised of samples from members that are interleaved in time with Wapshilla Ridge, likely requiring mechanically distinct pathways of magma transport through the crust even during Wapshilla Ridge emplacement and persistent recharge. Later groups within the Wanapum and Saddle Mountains appear to share similarities with Grande Ronde members (for example cluster 12 with Birch Creek, cluster 13 with Wapshilla Ridge, and clusters 18 and 19 with Sentinel Bluffs). Reuse of crustal structures and remobilization/mixing of older magma by subsequent members could help explain the known variability in Saddle Mountain members (Hooper, 2000; Reidel et al., 2002, 2013). Although the Saddle Mountains largely occupy a distinct compositional space than prior lavas, overlap in GMM clusters between small percentages of other Formations (including apparent mixing of American Bar with several Saddle Mountains members in cluster 17) suggests residual fluxing of

magma through these increased storage zones left from the main phase eruptions. Clusters 16 (dominantly Asotin) and 18 (Weissenfels Ridge and Ice Harbor with a few samples from Sentinel Bluffs) could plausibly reflect a FC or RAFC trend in Fig. 17.C-D from Picture Gorge dominated primitive compositions (cluster 4). The trend overall across all members seems to push early primitive compositions to more evolved compositions through assimilation and fractional crystallization to varying degrees, and then later compositions appear to reflect a recharge driven return to more primitive compositions and further FC and AFC to create large variations in composition in the later stages of the eruptive activity (Figure 17.C,D).

Taking an onset age for the CRFB at 16.9 Ma (Kasbohm et al., 2023), eruption rate for the cumulative ~42,800 km^3 of lava prior (spanning Steens, Imnaha, and early N1 magnetic polarity Grande Ronde members) to cluster 6 would be ~0.12 km^3/yr, similar to the long-term average modern eruption rate of the Hawaiian hotspot (Lipman and Calvert, 2013). Similarly, if we examine the latter part of the Grande Ronde constrained by the Kasbohm et al., (2023) ages (Fields Spring member on) not encompassed by our clusters 6-9 and 11 through the end of the Wanapum (Priest Rapids member), ~27,500 km^3 erupted volume is associated with 297 kyr and the implied average eruption rate is ~0.09 km^3/yr.

The later eruption rates of R2 magnetic polarity Grande Ronde lavas through Imnaha thus appear smaller (although similar in magnitude) to that leading up to the middle Grande Ronde members. And the compositions of GMM clusters associated with transitional members entering and leaving the Grande Ronde (clusters #3-4 and #12-13) plot together for some elements (e.g., Fig 17.B,D) but not others (e.g., Fig. 17.C), which may indicate either post-depositional alteration, or similarities driven by similar magmatic processes affecting the beginning of the eruptive phase and the waning end of Grande Ronde activity. Consideration of magma storage dynamics suggest that the thermal legacy of a large mantle melt pulse and assimilation episode is a shift towards increased storage, so we speculate that the sharp decrease in eruption rates seen at the end of the Grande Ronde reflects a decrease in the efficacy of the crust to transmit magma (e.g., Black et al., 2024). We also note that the only notable hiatus identified in CRFB main phase volcanism by the dating of Kasbohm et al., (2023) occurs at the end of Grande Ronde time, which is consistent with (although not uniquely explained by) a shift in crustal storage capacity.

In the context of ML for igneous processes generally, it is notable that we in this section have returned to 'traditional' methods, relying on element- or ratio-wise comparisons with expectations for a given RAFC scenario (using bivariate diagrams) to interpret patterns of GMM clusters as a visualization bridge between traditional petrologic analysis and automated multidimensional analysis. Because the Magma Chamber Simulation and other similar tools predict the full suite of major and trace elements, it should be possible to derive RAFC interpretations for petrologic evolution involving all features simultaneously in a ML framework (e.g., (Till, 2025). Ideally, thermodynamic evolution is itself constrained by mechanical models of eruption cycles, in which mass and energy transfer associated with recharge and evacuation from magma storage zones are physically self-consistent with the rheologic evolution of the crust (e.g., (Karlstrom et al., 2017). We however leave this development to future work.

5.3 Conclusions

We have developed a combined supervised and unsupervised machine learning workflow for classification of high dimensional geochemical data, based on Multinomial Logistic Regression and Gaussian Mixture Models. This workflow (Fig. 6) provides a powerful framework for classification that can be leveraged to robustly and quantitatively characterize petrologic datasets generally, but here we exclusively study the Columbia River Flood Basalts. We compile a large database (N=7,975) of labeled published and unpublished whole rock analyses, systematically exploring supervised classification and then unsupervised clustering. The results of this exercise identify cryptic patterns that span the established CRFB stratigraphy and provide insight into the complex and time-evolving mantle source and crustal pathways that led to the observed eruption sequence, fingerprinting the geochemical life cycle of the CRFB.

Overall, our interpretation both at Formation and member level is of sudden expansion of crustal differentiation pathways in the N1 paleomagnetic phase of the Grande Ronde Formation, which likely indicates a transition in the mode of crustal transport associated with increased flux and thermal/rheologic priming that ultimately ended the massive eruptions of the main phase (Karlstrom and Richards, 2011). Mantle recharge signatures throughout the CRFB stratigraphy suggests that pre- as well as post-main phase eruptions established new pathways through the crust but also likely interacted episodically with pre-existing, and likely compartmentalized (e.g., Mittal and Richards, 2021a), storage regions. Further unraveling this complex sequence is

critical for understanding the life cycle of the CRFB and other flood basalts, and we hope that the tools developed here will aid in this effort.

ACKNOWLEDGEMENTS

We thank the University of Oregon Department of Earth Sciences for the institutional support that made this research possible and acknowledge funding from NSF CAREER 1848554 and 2317936 to L.K. Felicia Cummings was a crucial part of collecting and compiling the early stages of our database assembly and we therefore thank her for her contribution to this work. In addition to logistical and financial support, we are also grateful to Dr. Steve Reidel, Dr. Terry Tolan, Dr. John Wolff, Dr. Emily Cahoon, Dr. Ray Wells, Dr. Eugene Humphreys, Dr. Anita Grunder and Dr. Martin Streck for sharing data and insights on the stratigraphy of the Columbia River Flood Basalts. All code associated with this paper, including scripts to use the MLR models for classification, may be found at https://github.com/leifkarlstrom/CRB_ml_classifiers .

REFERENCES

Aitchison, J., 1983, Principal Component Analysis of Compositional Data: Biometrika, v. 70, p. 57–65.

Aitchison, J., Barcelo-Vidal, C., and Pawlowsky-Glahn, V., 1993, Some Comments on Compositional Data Analysis Archaeometry, In Particular the Fallacies in Tangri and Wright's Dismissal of Logratio Analysis: , p. 1–20.

Arrowsmith, S.J., Trugman, D.T., MacCarthy, J., Bergen, K.J., Lumley, D., and Magnani, M.B., 2022, Big Data Seismology: Reviews of Geophysics, v. 60, p. 1–55, doi:10.1029/2021RG000769.

Audunsson, H., and Levi, S., 1997, Geomagnetic fluctuations during a polarity transition: Journal of Geophysical Research, v. 102.

Azari, A. et al., 2021, Integrating Machine Learning for Planetary Science: Perspectives for the Next Decade: Bulletin of the AAS, v. 53, doi:10.3847/25c2cfeb.aa328727.

Baker, L.L., Camp, V.E., Reidel, S.P., Martin, B.S., Ross, M.E., and Tolan, T.L., 2019,

Alteration, mass analysis, and magmatic compositions of the Sentinel Bluffs Member, Columbia River flood basalt province: COMMENT: Geosphere, v. 15, p. 1436–1447, doi:10.1130/GES02047.1.

Barry, T.L., Kelley, S.P., Camp, V.E., Self, S., Jarboe, N.A., and Duncan, R.A., 2013, Eruption chronology of the Columbia River Basalt Group: Geological Society of America Special Papers, v. 2497, p. 45–66, doi:10.1130/2013.2497(02).

Biasi, J.A., 2021, Paleomagnetism and Geochemistry of Basalts in the North American Cordillera , Davis Strait , and Antarctica Thesis by: C-1-C–89 p.

Biasi, J., and Karlstrom, L., 2021, Timescales of magma transport in the Columbia River flood basalts, determined by paleomagnetic data: Earth and Planetary Science Letters, v. 576, p. 117169, doi:10.1016/j.epsl.2021.117169.

Black, B.A., Karlstrom, L., and Mather, T.A., 2021, The life cycle of large igneous provinces: Nature Reviews Earth and Environment, v. 2, p. 840–857, doi:10.1038/s43017-021-00221-4.

Bohrson, W.A., and Spera, F.J., 2001, Energy-constrained open-system magmatic processes II: Application of energy-constrained assimilation fractional crystallization (EC-AFC) model to magmatic systems: Journal of Petrology, v. 42, p. 1019–1041.

Bohrson, W.A., Spera, F.J., Ghiorso, M.S., Brown, G.A., Creamer, J.B., and Mayfield, A., 2014, Thermodynamic model for energy-constrained open-system evolution of crustal magma bodies undergoing simultaneous recharge, assimilation and crystallization: The magma chamber simulator: Journal of Petrology, doi:10.1093/petrology/egu036.

Bond, D.P.G., and Wignall, P.B., 2014, Large igneous provinces and mass extinctions: An update: Special Paper of the Geological Society of America, v. 505, p. 29–55, doi:10.1130/2014.2505(02).

Boschetty, F.O., Ferguson, D.J., Cortés, J.A., Morgado, E., Ebmeier, S.K., Morgan, D.J., Romero, J.E., and Silva Parejas, C., 2022, Insights Into Magma Storage Beneath a Frequently Erupting Arc Volcano (Villarrica, Chile) From Unsupervised Machine Learning Analysis of Mineral Compositions: Geochemistry, Geophysics, Geosystems, v. 23, p. 1–24,

doi:10.1029/2022gc010333.

Box, G.E.P., and Cox, D.R., 1964, An Analysis of Transformations: Journal of the Royal Statistical Society: Series B (Methodological), v. 26, p. 211–252, doi:10.1111/j.2517-6161.1964.tb00553.x.

Bryan, S.E., and Ferrari, L., 2013, Large igneous provinces and silicic large igneous provinces: Progress in our understanding over the last 25 years: Bulletin of the Geological Society of America, v. 125, p. 1053–1078, doi:10.1130/B30820.1.

Bush, J., Dunlap, P., and Reidel, S., 2018, Miocene evolution of the Moscow-Pullman Basin, Idaho and Washington (Technical Report 18-3).:

Bush, J., Garwood, D., and Kauffman, J., 2005, Geologic map of the Lapwai quadrangle, Nez Perce County, Idaho (Digital Web Map DWM-41).:

Bush, J., Garwood, D., Lewis, R., and McClelland, W., 2001, Bedrock geologic map of the Green Knob quadrangle, Latah and Nez Perce Counties, Idaho (Geologic Map 31).:

Bush, J., Kauffman, J., and Schmidt, K., 2004, Geologic map of the Craigmont quadrangle, Lewis and Idaho Counties, Idaho (Digital Web Map DWM-27).:

Cahoon, E.B., 2020, Distribution, Geochronology, and Petrogenesis of the Picture Gorge Basalt with Special Focus on Petrological Relationships to the Main Columbia River Basalt Group: 9–197 p.

Cahoon, E.B., Streck, M.J., and Ferns, M., 2021, Flood basalts, rhyolites, and subsequent volcanism of the Columbia River magmatic province in eastern Oregon, USA: Geological Society of America Field Guide, v. 62, p. 73–80, doi:10.1130/2021.0062(08).

Cahoon, E.B., Streck, M.J., and Koppers, A.A.P., 2023, Picture Gorge Basalt: Internal stratigraphy, eruptive patterns, and its importance for understanding Columbia River Basalt Group magmatism: Geosphere, v. 19, p. 406–430, doi:10.1130/GES02508.1.

Cahoon, E.B., Streck, M.J., Koppers, A.A.P., and Miggins, D.P., 2020, Reshuffling the Columbia river basalt chronology-picture gorge basalt, the earliest-and longest-erupting formation: Geology, v. 48, p. 348–352, doi:10.1130/G47122.1.

Camp, V.E., 2013, Origin of Columbia River Basalt: Passive rise of shallow mantle, or active upwelling of a deep-mantle plume? Geological Society of America Special Paper, v. 497, p. 181–199, doi:10.1130/2013.2497(07).

Camp, V.E., Reidel, S.P., Ross, M.E., Brown, R.J., and Self, S., 2017a, Field-Trip Guide to the Vents , Dikes , Stratigraphy , and Structure of the Columbia River Basalt Group , Eastern Oregon and Southeastern Washington: Scientific Investigations Report 2017-5022-N, p. 88 p., doi:10.1002/hbm.20105.

Camp, V.E., Ross, M.E., Duncan, R.A., Jarboe, N.A., Coe, R.S., Hanan, B.B., and Johnson, K., 2013, The Steens basalt: Earliest lavas of the Columbia River basalt group: The Columbia River Flood Basalt Province: Geological Society of America Special Paper 497, v. 2497, p. 87–116, doi:10.1130/2013.2497(04).

Camp, V.E., Ross, M.E., Duncan, R.A., and Kimbrough, D.L., 2017b, Uplift, rupture, and rollback of the Farallon slab reflected in volcanic perturbations along the Yellowstone adakite hot spot track: Journal of Geophysical Research: Solid Earth, p. 1–20, doi:10.1002/2016JB013849.

Caprarelli, G., and Reidel, S.P., 2004, Physical evolution of Grande Ronde Basalt magmas, Columbia River Basalt Group, north-western USA: Mineralogy and Petrology, v. 80, p. 1–25, doi:10.1007/s00710-003-0017-1.

de Caritat, P., and Grunsky, E.C., 2013, Defining element associations and inferring geological processes from total element concentrations in Australian catchment outlet sediments: Multivariate analysis of continental-scale geochemical data: Applied Geochemistry, doi:10.1016/j.apgeochem.2013.02.005.

Carniel, R., and Guzman, S.R., 2012, Machine Learning in Volcanology: A Review: IntechOpen, v. Updates in, p. 1–27, http://dx.doi.org/10.1039/C7RA00172J%0Ahttps://www.intechopen.com/books/advanced-biometric-technologies/liveness-detection-in-biometrics%0Ahttp://dx.doi.org/10.1016/j.colsurfa.2011.12.014.

Chen, S., Grunsky, E.C., Hattori, K., and Liu, Y., 2015, Principal Component Analysis of

Geochemical Data from the REE-rich Maw Zone, Athabasca Basin, Canada: Geological Survey of Canada, v. Open File, p. 1–21, doi:10.4095/295615.

Clarke, F.W., 1920, The Data of Geochemistry: Washington D.C., U.S. Geological Survey.

Conlon, T., 2020a, Columbia River Basalt Stratigraphy in the Pacific Northwest: Oregon Water Science Center,.

Conlon, T., 2020b, CRBG Stratigraphic Nomenclature Chart: Columbia River Basalt Stratigraphy in the Pacific Northwest, https://or.water.usgs.gov/projs_dir/crbg/nomenclature.png.

Conlon, T., 2020c, Sources of Information on CRBG Stratigraphy: Columbia River Basalt Stratigraphy in the Pacific Northwest,.

Conrey, R., Beard, C., and Wolff, J., 2013, Columbia River Basalt flow Stratigraphy in the Palouse Basin.:

Cruz, M., and Streck, M.J., 2022, The Castle Rock and Ironside Mountain calderas, eastern Oregon, USA: Adjacent venting sites of two Dinner Creek Tuff units—the most widespread tuffs associated with Columbia River flood basalt volcanism: GSA Bulletin, p. 1–21, doi:10.1130/b36070.1.

Dangeti, P., 2017, Statistics for Machine Learning: Techniques for exploring supervised, unsupervised, and reinforcement learning models with Python and R:

Davis, K.N., Wolff, J.A., Rowe, M.C., and Neill, O.K., 2017, Sulfur release from main-phase Columbia River Basalt eruptions: v. 45, p. 1043–1046, doi:10.1130/G39371.1.

Day, J.M.D., Nutt, K.L.R., Mendenhall, B., and Peters, B.J., 2021, Temporally variable crustal contributions to primitive mantle-derived Columbia River Basalt Group magmas: Chemical Geology, v. 572, doi:10.1016/j.chemgeo.2021.120197.

Dempster, A.P., Laird, N.M., and Rubin, D.B., 1976, Maximum Likelihood from Incomplete Data via the EM Algorithm: Journal of the Royal Statistical Society, v. 46, p. 139–144, doi:10.1115/1.3424485.

Derkey, R., and Hamilton, M., 2007, Geologic map of the Four Mound Prairie 7.5-minute

quadrangle, Spokane and Stevens Counties, Washington (Geologic Map GM-66).:

Derkey, R., Hamilton, M., and Stradling, D., 2004, Geologic map of the Airway Heights 7.5-minute quadrangle, Spokane County, Washington (Open File Report 2004-1).:

Derkey, R., Hamilton, M., Stradling, D., and Kiver, E., 1999, Preliminary geologic map of the Spokane SE 7.5-minute quadrangle, Spokane County, Washington (Open File Report 99-6).:

Dinterman, P.A., and Duvall, A.R., 2009, Preliminary geologic map of the Buxton 7.5' quadrangle, Washington County, Oregon: U.S. Geological Survey Open-File Report 2009-1186, v. scale 1:24,000.

Dodson, A., Kennedy, B.M., and DePaolo, D.J., 1997, Helium and neon isotopes in the Imnaha Basalt, Columbia River Basalt Group: Evidence for a Yellowstone plume source: Earth and Planetary Science Letters, v. 150, p. 443–451, doi:10.1016/S0012-821X(97)00090-3.

Dominguez, A.R., and Van der Voo, R., 2014, Secular variation of the middle and late Miocene geomagnetic field recorded by the Columbia River Basalt Group in Oregon, Idaho and Washington, USA: Geophysical Journal International, v. 197, p. 1299–1320, doi:10.1093/gji/ggt487.

EarthRef.org, 2019, Geochemical Earth Reference Model (GERM) database: https://earthref.org/GERM/,.

Ellefsen, K.J., Smith, D.B., and Horton, J.D., 2014, A modified procedure for mixture-model clustering of regional geochemical data: Applied Geochemistry, v. 51, p. 315–326, doi:10.1016/j.apgeochem.2014.10.011.

Ernst, R.E., 2014, Large Igneous Provinces: Cambridge University Press, doi:10.1017/CBO9781139025300.

Ernst, R.E., and Buchan, K.L., 1997, Giant radiating dyke swarms: Their use in identifying pre-Mesozoic large igneous provinces and mantle plumes: Geophysical Monograph Series, v. 100, p. 297–333, doi:10.1029/GM100p0297.

Evarts, B.R.C., 2004a, Geologic Map of the Saint Helens Quadrangle, Columbia County,

Oregon, and Clark and Cowlitz Counties, Washington: USGS Scientific Investigations, v. Map 2834, p. 1–24.

Evarts, R.C., 2004b, Geologic Map of the Woodland Quadrangle, Clark and Cowlitz Counties, Washington: Scientific Investigations Map, v. 2827, http://pubs.er.usgs.gov/publication/sim2827.

Evarts, R.C., and Fleck, R.J., 2017, Geologic Map of the Beacon Rock Quadrangle, Skamania County, Washington: USGS Scientific Investigations Map 3367,.

Evarts, R.C., O'Connor, J.E., and Tolan, T.L., 2013, Geologic Map of the Washougal Quadrangle, Clark County, Washington, and Multnomah County, Oregon: U.S. Geological Survey Scientific Investigations Map 3017, v. 3257, p. 32.

Ferns, M., 1999, Geologic map of the Fly Valley quadrangle, Union County, Oregon (Geologic Map Series GMS-113).:

Ferns, M., 2002, Geologic map of the Imbler quadrangle, Union County, Oregon (Geologic Map Series GMS-114).:

Ferns, M., and Madin, I., 1999, Geologic map of the Summerville quadrangle, Union County, Oregon (Geologic Map Series GMS-111).:

Ferns, M., and McConnell, V., 2005, Oregon geologic data compilation (northeast Oregon) (OGDC-1).:

Ferns, M., and McConnell, V., 2015, Oregon geologic data compilation (northeast Oregon) (OGDC-6).:

Field, A., 2013, Discovering Statistics Using IBM SPSS Statistics: SAGE Publications.

Filzmoser, P., Hron, K., and Reimann, C., 2009, Principal component analysis for compositional data with outliers: , p. 621–632, doi:10.1002/env.

Gard, M., Hasterok, D., and Halpin, J.A., 2019, Global whole-rock geochemical database compilation: Earth System Science Data, v. 11, p. 1553–1566, doi:10.5194/essd-11-1553-2019.

Garwood, D., and Bush, J., 2005, Geologic map of the Lewiston Orchards North quadrangle and

part of the Clarkston quadrangle, Nez Perce County, Idaho (Digital Web Map DWM-40).:

Garwood, D., Schmidt, K., Kauffman, J., Stewart, D., Lewis, R., Othberg, K., and Wampler, P., 2008, Geologic map of the White Bird quadrangle, Idaho County, Idaho (Digital Web Map DWM-101).:

Gaschnig, R.M., Vervoort, J.D., Lewis, R.S., and Tikoff, B., 2011, Isotopic evolution of the idaho batholith and Challis intrusive province, Northern US Cordillera: Journal of Petrology, v. 52, p. 2397–2429, doi:10.1093/petrology/egr050.

Geron, A., 2017, Hands-On Machine Learning With Scikit-Learn And TensorFlow: Concepts, Tools, And Techniques To Build Intelligent Systems:

Geshi, N., and Neri, M., 2014, Dynamic feeder dyke systems in basaltic volcanoes: the exceptional example of the 1809 Etna eruption (Italy): Frontiers in Earth Science, v. 2, doi:10.3389/feart.2014.00013.

Ghiorso, M.S., and Sack, R., 1995, Chemical mass transfer in magmatic processes IV: Contributions to Mineralogy and Petrology, v. 119, p. 197–212, doi:10.1007/BF00307281.

Gibson, I.., 1969, A comparative account of the fl ood basalt volcanism of the Columbia Plateau and eastern Iceland: Bulletin of Volcanology, v. 33, p. 420–437.

Gunn, B., and Watkins, N., 1970, Geochemistry of the Steens Mountain Basalts, Oregon: GSA Bulletin, v. 81, p. 1497–1516.

Hampton, R.L., 2022, From Isotopes and Whole Rock Geochemistry to Machine Learning: Diving into the Plumbing System of Large Mafic Eruptions Using a Diverse Geochemical Toolset to Investigate Magmatic Processes: University of Oregon.

Hartigan, J.A., and Hartigan, P.M., 1985, The Dip Test of Unimodality: The Annals of Statistics, v. 13, p. 70–84.

Hastie, T., Tibshirani, R., and Friedman, J., 2001, The Elements of Statistical Learning: v. 26, 505–516 p.

Hastie, W.W., Watkeys, M.K., and Aubourg, C., 2014, Magma flow in dyke swarms of the Karoo LIP: Implications for the mantle plume hypothesis: Gondwana Research, v. 25, p.

736–755, doi:10.1016/j.gr.2013.08.010.

Holtzman, B.K., Paté, A., Paisley, J., Waldhauser, F., and Repetto, D., 2018, Machine learning reveals cyclic changes in seismic source spectra in Geysers geothermal field: Science Advances, v. 4, doi:10.1126/sciadv.aao2929.

Hooper, P.R., 2000, Chemical discrimination of Columbia River Basalt Flows: Geochemistry, Geophysics, Geosystems, v. 1, doi:10.1029/2000GC000040.

Hooper, P.R., Camp, V.E., Reidel, S.P., and Ross, M.E., 2007, The origin of the Columbia River flood basalt province: Plume versus nonplume models: Geological Society of America, 635–668 p., doi:10.1130/2007.2430(30).

Hooper, P.R., and Hawkesworth, C.J., 1993, Isotopic and Geochemical Constraints on the Origin and Evolution of the Columbia River Basalt: Journal of Petrology, v. 34, p. 1203–1246.

Howarth, R.J., and Earle, S.A.M., 1979, Application of a generalized power transformation to geochemical data: Journal of the International Association for Mathematical Geology, v. 11, p. 45–62, doi:10.1007/BF01043245.

Hughes, G., 1968, On the mean accuracy of statistical pattern recognizers: IEEE Transactions on Information Theory, v. 14, p. 55–63, doi:10.1109/TIT.1968.1054102.

Itano, K., Ueki, K., Iizuka, T., and Kuwatani, T., 2020, Geochemical discrimination of monazite source rock based on machine learning techniques and multinomial logistic regression analysis: Geosciences (Switzerland), v. 10, doi:10.3390/geosciences10020063.

Iwamori, H., Yoshida, K., Nakamura, H., Kuwatani, T., Harnada, M., Haraguchi, S., and Ueki, K., 2017, Classification of geochemical data based on multivariate statistical analyses: Complementary roles of cluster, principal component, and independent component analyses: Geochemistry, Geophysics, Geosystems, v. 18, p. 994–1012, doi:10.1002/2016GC006663.Received.

Jarboe, N.A., Coe, R.S., Renne, P.R., and Glen, J.M.G., 2010, The age of the Steens reversal and the Columbia River Basalt Group: Chemical Geology, v. 274, p. 158–168, doi:10.1016/j.chemgeo.2010.04.001.

Jutzeler, M., Carey, R.J., Dagasan, Y., McNeill, A., and Cas, R.A.F., 2024, Machine-learning crystal size distribution for volcanic stratigraphy correlation: Scientific Reports, v. 14, p. 31793, doi:10.1038/s41598-024-82847-0.

Karlstrom, L., Murray, K.E., and Reiners, P.W., 2019, Bayesian markov-chain monte carlo inversion of low-temperature thermochronology around two 8 − 10 m wide columbia river flood basalt dikes: Frontiers in Earth Science, v. 7, doi:10.3389/feart.2019.00090.

Karlstrom, L., Paterson, S.R., and Jellinek, A.M., 2017, A reverse energy cascade for crustal magma transport: Nature Geoscience, v. 10, doi:10.1038/NGEO2982.

Karlstrom, L., and Richards, M., 2011, On the evolution of large ultramafic magma chambers and timescales for flood basalt eruptions: Journal of Geophysical Research, v. 116, p. B08216, doi:10.1029/2010JB008159.

Karlstrom, L., Rudolph, M.L., and Manga, M., 2012, Caldera size modulated by the yield stress within a crystal-rich magma reservoir: Nature Geoscience, v. 5, p. 402–405, doi:10.1038/ngeo1453.

Kasbohm, J., and Schoene, B., 2018, Rapid eruption of the Columbia River flood basalt and correlation with the mid-Miocene climate optimum: , p. 1–8.

Kasbohm, J., Schoene, B., Mark, D.F., Murray, J., Reidel, S., Szymanowski, D., Barfod, D., and Barry, T., 2023, Eruption history of the Columbia River Basalt Group constrained by high-precision U-Pb and 40Ar/39Ar geochronology: Earth and Planetary Science Letters, v. 617, p. 118269, doi:10.1016/j.epsl.2023.118269.

Katona, J., Fu, X., Mittal, T., Manga, M., and Self, S., 2021, Some Lava Flows May Not Have Been as Thick as They Appear: Geophysical Research Letters, v. 48, doi:10.1029/2021GL095202.

Kauffman, J., Lewis, R., Stewart, D., and Schmidt, K., 2008, Geologic map of the Goodwin Meadows quadrangle, Idaho County, Idaho (Digital Web Map DWM-102).:

Kauffman, J., Schmidt, K., Lewis, R., Stewart, D., Othberg, K., and Garwood, D., 2011, Geologic map of the McKinzie Creek quadrangle, Idaho County, Idaho (Digital Web Map DWM-123).:

Kubo Hutchison, A., Karlstrom, L., and Mittal, T., 2023, Multiscale Spatial Patterns in Giant Dike Swarms Identified Through Objective Feature Extraction: Geochemistry, Geophysics, Geosystems, v. 24, doi:10.1029/2022GC010842.

Lacassie, J.P., Solar, J.R., Roser, B., and Hervé, F., 2006, Visualization of volcanic rock geochemical data and classification with artificial neural networks: Mathematical Geology, v. 38, p. 697–710, doi:10.1007/s11004-006-9042-z.

Lee, D.D., and Seung, H.S., 2000, Learning the parts of objects by non-negative matrix factorization: v. 401, p. 788–791.

Lerner, A.H. et al., 2021, The petrologic and degassing behavior of sulfur and other magmatic volatiles from the 2018 eruption of Kīlauea, Hawai‘i: melt concentrations, magma storage depths, and magma recycling: Springer Berlin Heidelberg, v. 83, 1–32 p., doi:10.1007/s00445-021-01459-y.

Leys, C., Ley, C., Klein, O., Bernard, P., and Licata, L., 2013, Detecting outliers: Do not use standard deviation around the mean, use absolute deviation around the median: Journal of Experimental Social Psychology, v. 49, p. 764–766, doi:10.1016/j.jesp.2013.03.013.

Lipman, P.W., and Calvert, A.T., 2013, Modeling volcano growth on the Island of Hawaii: Deep-water perspectives: Geosphere, v. 9, p. 1348–1383, doi:10.1130/GES00935.1.

Lubbers, J., Loewen, M., Wallace, K., Coombs, M., and Addison, J., 2023, Probabilistic Source Classification of Large Tephra Producing Eruptions Using Supervised Machine Learning: An Example From the Alaska-Aleutian Arc: Geochemistry, Geophysics, Geosystems, v. 24, doi:10.1029/2023GC011037.

Madhukar, M., 2019, Big Data for Remote Sensing: Visualization, Analysis and Interpretation: Digital Earth and Smart Earth: 129–154 p., doi:10.1007/978-3-319-89923-7_5.

Madin, I., 2004, Geologic map of the Fort Klamath quadrangle, Klamath County, Oregon (Geologic Map Series GMS-96).:

Madin, I., and Niewendorp, C., 2008, Preliminary geologic map of the Dixie Mountain 7.5’ quadrangle, Columbia, Multnomah, and Washington Counties, Oregon (Open-File Report O-08-07):

Marsh, J.S., 1987, Basalt geochemistry and tectonic discrimination within continental flood basalt provinces: Journal of Volcanology and Geothermal Research, v. 32, p. 35–49, doi:10.1016/0377-0273(87)90035-7.

Martin, B.S., Tolan, T.L., and Reidel, S.P., 2013, Revisions to the stratigraphy and distribution of the Frenchman Springs Member, Wanapum Basalt, *in* The Columbia River Flood Basalt Province, Geological Society of America, doi:10.1130/2013.2497(06).

Mcdougall, I., 1976, Geochemistry and origin of basalt of the Columbia River Group, Oregon and Washington: Bulletin of the Geological Society of America, v. 87, p. 777–792, doi:10.1130/0016-7606(1976)87<777:GAOOBO>2.0.CO;2.

Mittal, T., and Richards, M.A., 2021, The Magmatic Architecture of Continental Flood Basalts: 2. A New Conceptual Model: Journal of Geophysical Research: Solid Earth, v. 126, doi:10.1029/2021JB021807.

Mittal, T., Richards, M.A., and Fendley, I.M., 2021, The Magmatic Architecture of Continental Flood Basalts I: Observations From the Deccan Traps: Journal of Geophysical Research: Solid Earth, v. 126, p. 1–54, doi:10.1029/2021JB021808.

Moore, N.E., Grunder, A.L., and Bohrson, W.A., 2018, The three-stage petrochemical evolution of the Steens Basalt (southeast Oregon , USA) compared to large igneous provinces and layered mafic intrusions: v. 14, p. 1–28, doi:10.1130/GES01665.1/4346436/ges01665.pdf.

Moore, N.E., Grunder, A.L., Bohrson, W.A., Carlson, R.W., and Bindeman, I.N., 2020, Changing Mantle Sources and the Effects of Crustal Passage on the Steens Basalt, SE Oregon: Chemical and Isotopic Constraints: Geochemistry, Geophysics, Geosystems, v. 21, p. 1–33, doi:10.1029/2020GC008910.

Norinder, U., and Norinder, P., 2022, Predicting Amazon customer reviews with deep confidence using deep learning and conformal prediction: Journal of Management Analytics, v. 9, p. 1–16, doi:10.1080/23270012.2022.2031324.

Oggier, F., Widiwijayanti, C., and Costa, F., 2023, Global volcanic rock classification of Holocene volcanoes: Scientific Data, v. 10, p. 422, doi:10.1038/s41597-023-02324-7.

Oregon Water Resources Department - Well log query tool Oregon State Government,

http://apps2.wrd.state.or.us/apps/gw/well_log/Default.aspx (accessed June 2025).

Pearce, J.A., Ernst, R.E., Peate, D.W., and Rogers, C., 2021, LIP printing: Use of immobile element proxies to characterize Large Igneous Provinces in the geologic record: Lithos, v. 392–393, p. 106068, doi:10.1016/j.lithos.2021.106068.

Pearce, J.A., Harris, N.B.W., and Tindle, A.G., 1984, Trace element discrimination diagrams for the tectonic interpretation of granitic rocks: Journal of Petrology, v. 25, p. 956–983, doi:10.1093/petrology/25.4.956.

Peck, R., Olsen, C., and Devore, J., 2005, Introduction to Statistics and Data Analsis:

Pedregosa et al., 2011, Scikit-learn: Machine Learning in Python: JMLR, p. 2825–2830.

Petcovic, H.L., and Dufek, J.D., 2005, Modeling magma flow and cooling in dikes: Implications for emplacement of Columbia River flood basalts: Journal of Geophysical Research: Solid Earth, v. 110, p. 1–15, doi:10.1029/2004JB003432.

Petcovic, H.L., and Grunder, A.L., 2003, Textural and thermal history of partial melting in tonalitic wallrock at the margin of a basalt dike, Wallowa Mountains, Oregon: Journal of Petrology, v. 44, p. 2287–2312, doi:10.1093/petrology/egg078.

Petrelli, M., and Perugini, D., 2016, Solving petrological problems through machine learning : the study case of tectonic discrimination using geochemical and isotopic data: Contributions to Mineralogy and Petrology, v. 171, p. 1–15, doi:10.1007/s00410-016-1292-2.

Pitcher, B.W., and Kent, A.J.R., 2019, Statistics and segmentation: Using Big Data to assess Cascades arc compositional variability: Geochimica et Cosmochimica Acta, v. 265, p. 443–467, doi:10.1016/j.gca.2019.08.035.

Pivarunas, A.F., Avery, M.S., Hagstrum, J.T., Bennett, S.E.K., and Calvert, A.T., 2025, New Paleomagnetic Constraints on the Eruption Timing, Stratigraphy, and Post-Emplacement Deformation of the Picture Gorge Basalt Within the Columbia River Basalt Group: Journal of Geophysical Research: Solid Earth, v. 130, doi:10.1029/2024JB030728.

Pouget, S., Bursik, M., Cortés, J.A., and Hayward, C., 2014, Use of principal component analysis for identi fi cation of Rockland and Trego Hot Springs tephras in the Hat Creek Graben ,

northeastern: Quaternary Research, v. 81, p. 125–137, doi:10.1016/j.yqres.2013.10.012.

Praus, P., 2005, SVD-based principal component analysis of geochemical data: Central European Journal of Chemistry, v. 3, p. 731–741, doi:10.2478/BF02475200.

Reidel, S.P., 2005, A lava flow without a source: The Cohassett flow and its compositional components, Sentinel Bluffs Member, Columbia River Basalt Group: Journal of Geology, v. 113, p. 1–21, doi:10.1086/425966.

Reidel, S.P., 1982, Stratigraphy of the Grande Ronde Basalt , Columbia River Basalt Group , From the Lower Salmon River and Northern Hells Canyon Area, Idaho, Oregon, and Washington: Idaho Bureau of Mines and Geology Bulletin, p. 77–101.

Reidel, S.P., 2015, The Columbia River Basalt Group: A Flood Basalt Province in the Pacific Northwest, USA: Geosciences Canada, v. 42, p. 151–168.

Reidel, S.P., Camp, V.E., Martin, B.S., Tolan, T.L., and Wolff, J.A., 2016, The Columbia River Basalt Group of western Idaho and eastern Washington-Dikes, vents, flows, and tectonics along the eastern margin of the flood basalt province: GSA Field Guides, v. 41, p. 127–150, doi:10.1130/2016.0041(04).

Reidel, S.P., Camp, V.E., Tolan, T.L., and Martin, B.S., 2013, The Columbia River flood basalt province : Stratigraphy , areal extent , volume , and physical volcanology: Special Paper of the Geological Society of America, v. 497, p. 1–43, doi:10.1130/2013.2497(01).

Reidel, S., Hooper, P., Webster, G., and Camp, V., 1992, Geologic map of southeastern Asotin County, Washington (Geologic Map GM-40).:

Reidel, S.P., Johnson, V.G., and Spane, F.A., 2002, Natural Gas Storage in Basalt Aquifers of the Columbia Basin , Pacific Northwest USA: A Guide to Site Characterization: Pacific Northwest National Laboratory, p. 277.

Reidel, S.P., and Tolan, T.L., 2013, The Grande Ronde Basalt, Columbia River Basalt Group, *in* The Columbia River Flood Basalt Province, Geological Society of America, doi:10.1130/2013.2497(05).

Reidel, S.P., and Tolan, T.L., 1989, The Grande Ronde Basalt, Columbia River Basalt Group -

Stratigraphic Descriptions and Correlations in Washington , Oregon, and ldaho: Special Paper of the Geological Society of America, v. 239, p. 21–53, doi:10.1130/SPE239-p21.

Rosenberg, A., and Hirschberg, J., 2007, V-Measure: A conditional entropy-based external cluster evaluation measure: EMNLP-CoNLL 2007 - Proceedings of the 2007 Joint Conference on Empirical Methods in Natural Language Processing and Computational Natural Language Learning, p. 410–420.

Rudnick, R.L., and Gao, S., 2003, Composition of the Continental Crust: Treatise on geochemistry, v. 3, p. 1–64.

Sawlan, M.G., 2019, Alteration, mass analysis, and magmatic compositions of the Sentinel Bluffs Member, Columbia River flood basalt province: REPLY: Geosphere, v. 15, p. 1448–1458, doi:10.1130/GES02047.1.

Sawlan, M.G., 2017, Alteration, mass analysis, and magmatic compositions of the Sentinel Bluffs Member, Columbia River flood basalt province: Geosphere, v. 14, p. 286–303, doi:10.1130/GES01188.1.

Schmidt, K., Garwood, D., and Kauffman, J., 2005, Geologic map of the Keuterville quadrangle, Lewis and Idaho Counties, Idaho (Digital Web Map DWM-38).:

Schmidt, K., Kauffman, J., Stewart, D., Lewis, R., Othberg, K., and Garwood, D., 2009, Geologic map of the Slate Creek quadrangle, Idaho County, Idaho (Digital Web Map DWM-108).:

Schuster, J., 1993, Geologic map of the Clarkston 1:100,000 quadrangle, Washington-Idaho, and the Washington portion of the Orofino 1:100,000 quadrangle (Open File Report 93-4).:

Sheldrake, T., Caricchi, L., and Scutari, M., 2020, Tectonic Controls on Global Variations of Large-Magnitude Explosive Eruptions in Volcanic Arcs: Frontiers in Earth Science, v. 8, doi:10.3389/feart.2020.00127.

Snavely, P.D., 1962, Tertiary Geologic History of Western Oregon and Washington: AAPG Bulletin, v. 46, doi:https://doi.org/10.1306/BC7437FF-16BE-11D7-8645000102C1865D.

Soderberg, E.R., and Wolff, J.A., 2023, Mantle source lithologies for the Columbia River flood

basalt province: Contributions to Mineralogy and Petrology, v. 178, p. 11, doi:10.1007/s00410-023-01993-2.

Streck, M.J., Fredenberg, L.J., Fox, L.M., Cahoon, E.B., and Mass, M.J., 2023, Province-Wide Tapping of a Shallow, Variably Depleted, and Metasomatized Mantle to Generate Earliest Flood Basalt Magmas of the Columbia River Basalt, Northwestern USA: Minerals, v. 13, p. 1544, doi:10.3390/min13121544.

Swanson, D.A., Vance, J.A., Clayton, G., and Evarts, R.C., 1989, Cenozoic volcanism in the Cascade Range and Columbia Plateau, southern Washington and northernmost Oregon : Seattle, Washington to Portland, Oregon, July 3-8, 1989: American Geophysical Union, v. Field Trip, p. 1–60.

Swanson, D.A., Wright, T.L., Hooper, P.R., and Bentley, R.D., 1979, Revisions in Stratigraphic Nomenclature of the Columbia River Basalt Group (No. 1457).:

Takahahshi, E., Nakajima, K., and Wright, T.L., 1998, Origin of the Columbia River basalts: Melting model of a heterogeneous plume head: Earth and Planetary Science Letters, v. 162, p. 63–80, doi:10.1016/S0012-821X(98)00157-5.

Templ, M., Filzmoser, P., and Reimann, C., 2008, Cluster analysis applied to regional geochemical data: Problems and possibilities: Applied Geochemistry, doi:10.1016/j.apgeochem.2008.03.004.

Till, C.B., 2025, Magmatic trees: a method to compare processes between igneous systems: Volcanica, v. 8, p. 135–157, doi:10.30909/vol.08.01.135157.

Trimble, D.E., 1963, Geology of Portland, Oregon and Adjacent Areas: Geological Society of America Bulletin, v. 1119, p. 247.

U.S. Geological Survey, 2019, Chemical analyses for Multnomah Falls core hole: Oregon Water Science Center,.

Ueki, K., Hino, H., and Kuwatani, T., 2018, Geochemical discrimination and characteristics of magmatic tectonic settings: A machine-learning-based approach: Geochemistry, Geophysics, Geosystems, v. 19, p. 1327–1347, doi:10.1029/2017GC007401.

Ueki, K., and Iwamori, H., 2017, Geochemical differentiation processes for arc magma of the Sengan volcanic cluster, Northeastern Japan, constrained from principal component analysis: Lithos, v. 290–291, p. 60–75, doi:10.1016/j.lithos.2017.08.001.

Vesselinov, V. V, Alexandrov, B.S., and Malley, D.O., 2018, Contaminant source identification using semi-supervised machine learning: Journal of Contaminant Hydrology, v. 212, p. 134–142, doi:10.1016/j.jconhyd.2017.11.002.

Vye-Brown, C., Barry, T.L., and Self, S., 2019, Revealing emplacement dynamics of a simple flood basalt eruption unit using systematic compositional heterogeneities, *in* Field Volcanology: A Tribute to the Distinguished Career of Don Swanson, Geological Society of America, p. 21–39, doi:10.1130/2018.2538(02).

Wang, X., Zhu, P., Kusky, T.M., Zhao, N., Li, X., and Wang, Z., 2016, Dynamic cause of marginal lithospheric thinning and implications for craton destruction: A comparison of the North China, Superior, and Yilgarn Cratons: Canadian Journal of Earth Sciences, v. 53, p. 1121–1141, doi:10.1139/cjes-2015-0110.

Waters, A.C., 1961, Stratigraphic and lithologic variations in the Columbia River Basalt: American Journal of Science, v. 259, p. 583–611.

Webb, B.M., Streck, M.J., McIntosh, W.C., and Ferns, M.L., 2019, The Littlefield Rhyolite and associated mafic lavas: Bimodal volcanism of the Columbia River magmatic province, with constraints on age and storage sites of Grande Ronde Basalt magmas: Geosphere, v. 15, p. 60–84, doi:10.1130/GES01695.1.

Wells, R.E. et al., 2020, Geologic Map of the Greater Portland Metropolitan Area and Surrounding Regions, Oregon and Washington: USGS Scientific Investigations, Map 3443, p. 359, doi:10.1130/abs/2019CD-329168.

Wells, R., Niem, A., Evarts, R., and Hagstrum, J., 2009, The Columbia River Basalt Group-From the gorge to the sea: The Geological Society of America, v. 15, p. 737–774, doi:10.1130/2009.fl.

White, W.M., 2013, Trace Elements in Igneous Processes, *in* Geochemistry, p. 259–313.

Wignall, P.B., 2001, Large igneous provinces and mass extinctions:

Wilson, R.L., and Watkins, N.D., 1967, Correlation of Petrology and Natural Magnetic Polarity in Columbia Plateau Basalts: Geophysical Journal of the Royal Astronomical Society, v. 12, p. 405–424, doi:10.1111/j.1365-246X.1967.tb03150.x.

Wolff, J.A., and Ramos, F.C., 2013, Source materials for the main phase of the Columbia River Basalt Group: Geochemical evidence and implications for magma storage and transport: Special Paper of the Geological Society of America, v. 497, p. 273–291, doi:10.1130/2013.2497(11).

Wolff, J.A., Ramos, F.C., Hart, G.L., Patterson, J.D., and Brandon, A.D., 2008, Columbia River flood basalts from a centralized crustal magmatic system: v. 704, p. 177–180, doi:10.1038/ngeo124.

Wright, T.L., Grolier, M.J., and Swanson, D.A., 1973, Chemical variation related to the stratigraphy of the Columbia river basalt: Bulletin of the Geological Society of America, v. 84, p. 371–386, doi:10.1130/0016-7606(1973)84<371:CVRTTS>2.0.CO;2.

Yu, X., Lee, C., Chen, L., and Zeng, G., 2015, Magmatic recharge in continental flood basalts:Insights from the Chifeng igneous province in Inner Mongolia: Geochemistry, Geophysics, Geosystems, p. 2082–2096, doi:10.1002/2015GC005805.Received.

Yuh, I.P., Evarts, R.C., and Conrey, R.M., 2022, X-ray Fluorescence Geochemistry of Columbia River Basalt Group Rocks in the Western Columbia River Gorge: U.S. Geological Survey data release,.

FIGURES

Age (Ma)	Formation (Volume in km³) #members	# Samples in database		
~6	Saddle Mountains (2,424) 11 members	1219	911	859
15.92	Wanapum (12,175) 5 members	1552	960	906
16.14	Grande Ronde (149,000) 24 members	2766	2286	2003
16.57	Picture Gorge* (<8,100) 1 member	138	138	138
	Imnaha (11,000) 4 members	374	195	183
16.64	Steens (31,800) 2 members	210	110	77
~16.9				

Database subset	# Samples	Element names	# Elements	# Features in database
D1	6259	SiO2,TiO2,Al2O3,MnO,MgO, CaO,Na2O,K2O,P2O5	9	45
D2	4600	SiO2,TiO2,Al2O3,MnO,MgO, CaO,Na2O,K2O,P2O5,Ni,Cr, Sc,V,Ba,Rb,Sr,Zr,Y,Nb,Cu	20	210
D3	4007	SiO2,TiO2,Al2O3,MnO,MgO, CaO,Na2O,K2O,P2O5,Ni,Cr, Sc,V,Ba,Rb,Sr,Zr,Y,Nb,Cu,Pb, La,Ce,Th,Ga	25	325

ID	Member	# Samples		
46	Lower Monumental	19	13	8
45	Ice Harbor	111	71	65
44	Buford	42	28	25
43	Elephant Mountain	79	51	48
42	Weippe	96	93	88
41	Pomona	59	44	41
40	Esquatzel	26	19	16
39	Weissenfels Ridge	149	110	101
38	Asotin	216	185	182
37	Wilber Creek	58	53	46
36	Umatilla	365	245	239
35	Priest Rapids	529	376	365
34	Roza	132	62	58
33	Shumaker Creek	111	57	54
32	Frenchman Springs	621	353	334
31	Eckler Mountain	158	111	95
30	Sentinel Bluffs	683	571	567
29	Winter Water	170	150	150
28	Field Springs	65	33	0
27	Indian Ridge	31	31	0
26	Armstrong Canyon	21	21	21
25	Ortley	88	79	79
24	Slack Canyon	13	7	3
23	Meyer Ridge	326	239	239
22	Grouse Creek	67	63	63
21	Wapshilla Ridge	767	600	558
20	Mount Horrible	38	38	38
19	Cold Springs Ridge	74	74	7
18	Hoskin Gulch	56	56	6
17	China Creek	48	40	40
16	Frye Point	17	17	5
15	Downey Gulch	77	59	59
14	Brady Gulch	21	21	2
13	Kendrik Grade	27	27	27
12	Center Creek	12	10	10
11	Skeleton Creek	38	38	5
10	Rogersburg	28	23	23
9	Teepee Butte	37	31	31
8	Birch Creek	38	38	17
7	Buckhorn Springs	24	20	20
6	Picture Gorge	138	138	138
5	Rock Creek	131	68	65
4	American Bar	187	99	96
3	Fall Creek	17	8	5
2	Log Creek	39	20	17
1	Upper Steens	89	32	16
0	Lower Steens	121	78	61

Figure 1: Stratigraphy of the CRFB and databases compiled in this work, based on Reidel and Tolan (2013) and Reidel et al., (2013), dates from Kasbohm et al., (2023) and Barry et al. (2013) for Saddle Mountains. Color scheme for Formations will be used throughout, as will numerical labels for members. Data subsets D1-D3 include differing numbers of trace elements, which changes the total number of samples and data features resulting from ratios of elements.

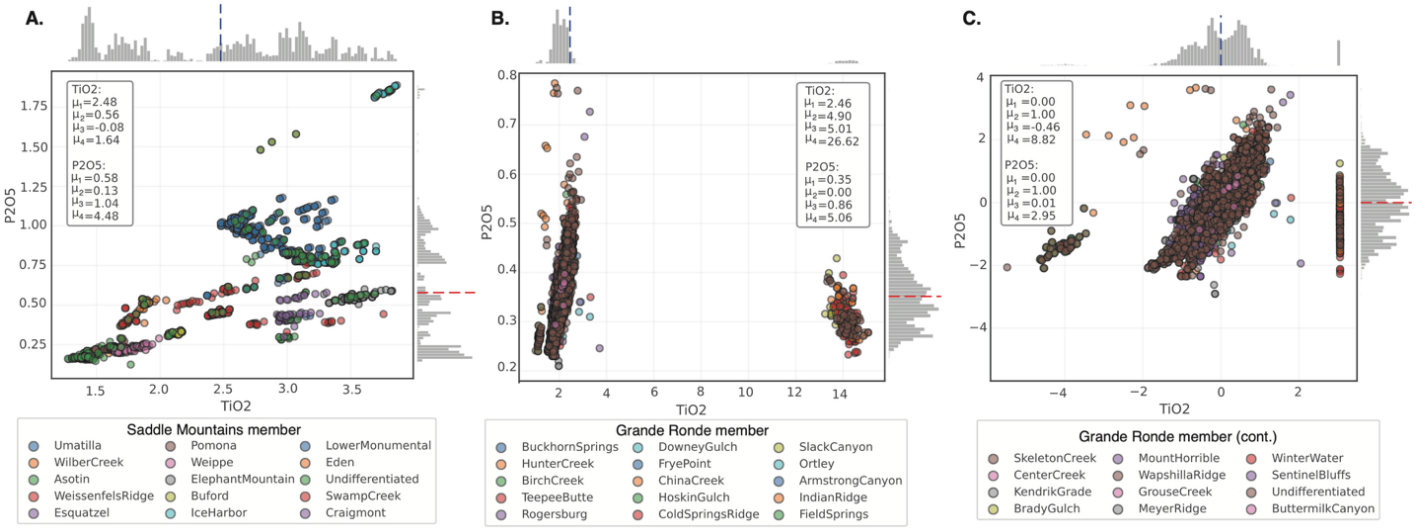

Figure 2: Biplots of TiO_2 versus P_2O_5 for **A.** Saddle Mountains Formation, **B.** Grande Ronde Formation, **C.** Same as (B) but after Box-Cox Power Transform. Histograms on top and right are projections of sample data, and the first four moments of these distributions are listed. The "Undifferentiated" label in both cases is the dataset we use as application of our ML classifier in Section 4.

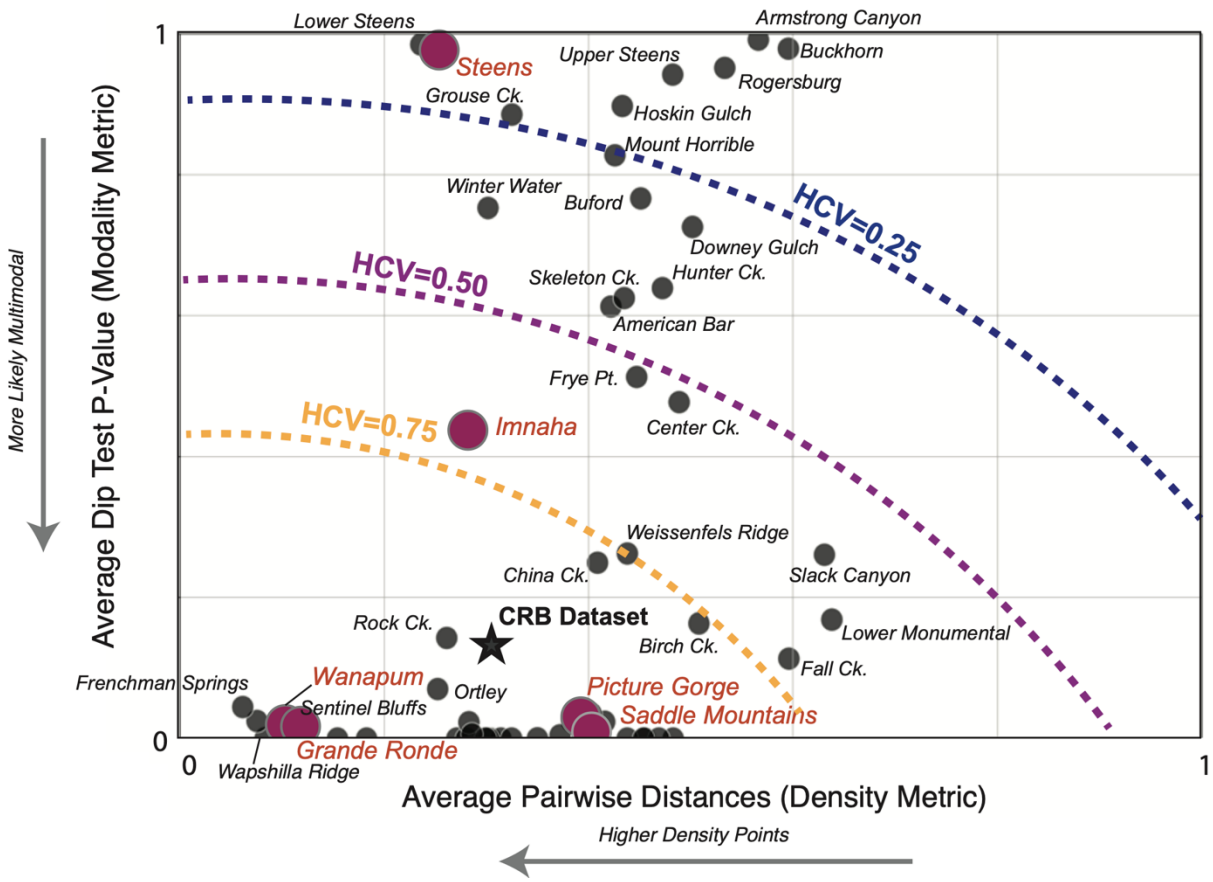

Figure 3: Regime diagram based on synthetic Gaussian data of "clusterability" based on the V score (known as the HCV metric in the Python Sci-Kit Learn library), as a function of average pairwise distance between all features and the p-value of the distribution of interest according to the Hartigan Dip Test (Hartigan and Hartigan, 1985). Members and Formations as well as CRFB dataset D2 are also plotted.

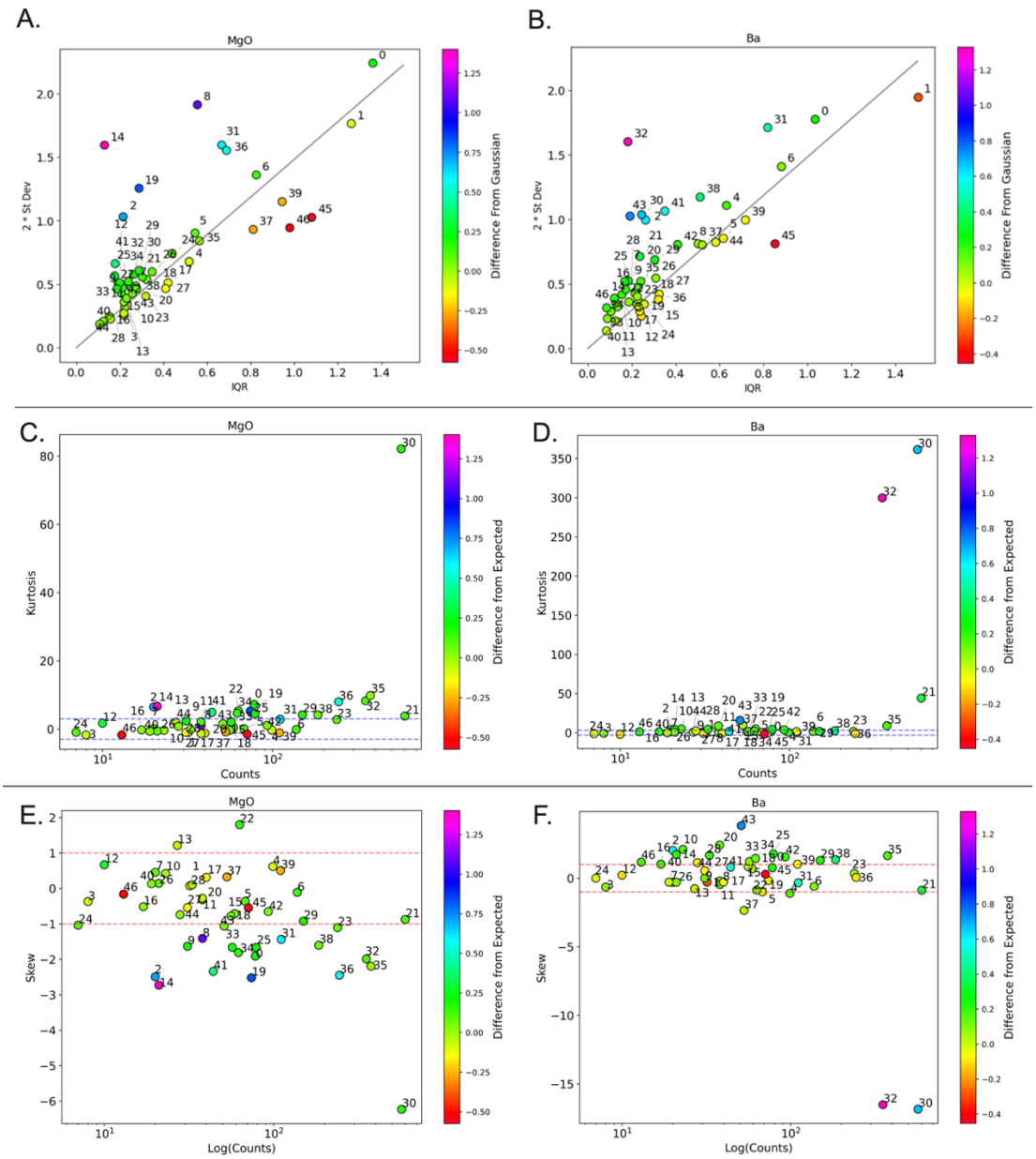

Figure 4: Member-wise moments compared to expected values from a Gaussian distribution, using MgO and Ba as representative major and trace elements. **A.** and **B.** IQR vs 2*second moment (μ_2) with the expected Gaussian line (IQR*1.4826) shown in grey and the difference from that expected as the colors. **C.** and **D.** Count in each member versus the Kurtosis (μ_4) with the color indicating the difference from the expected Gaussian line in column 1, and the expected Gaussian range of -3 to 3 shown by the dashed line (Field, 2013). E and F) Same analysis but with the Skewness (μ_3) and the Gaussian bounds between -1 and 1.

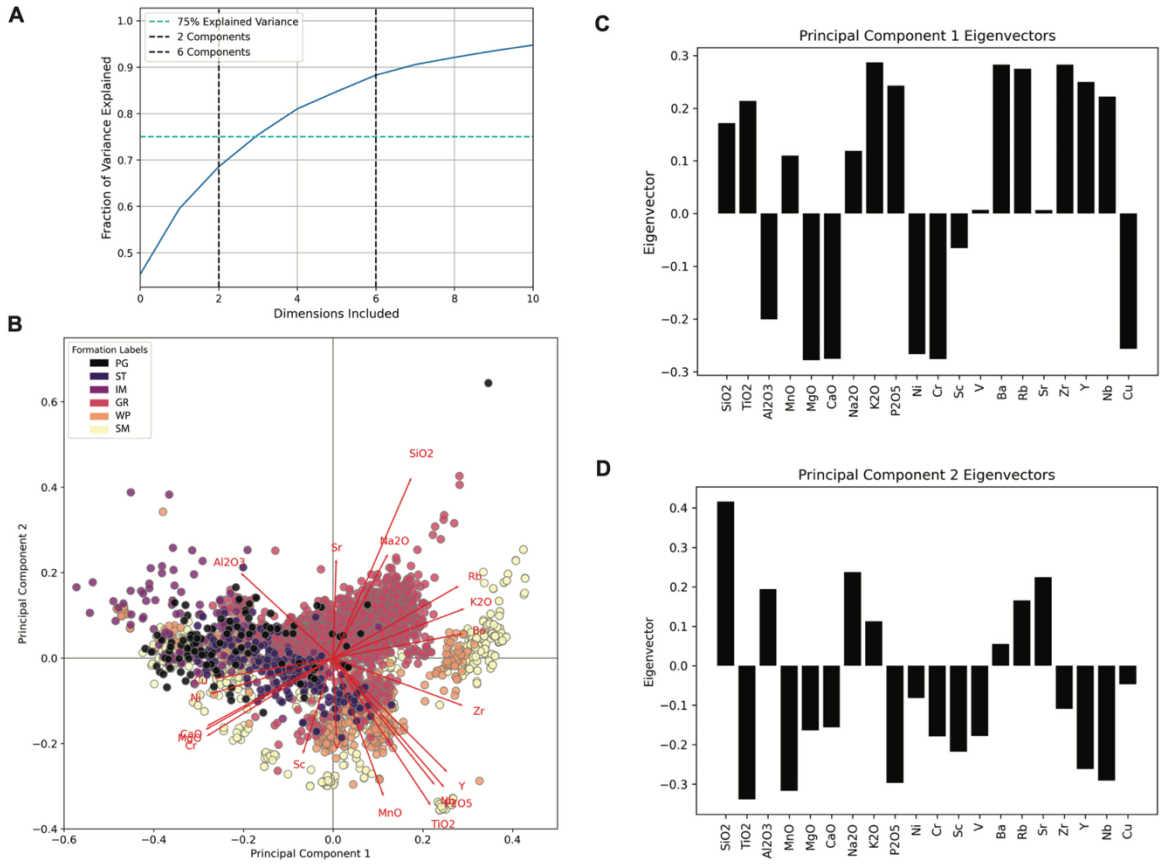

Figure 5: Principal Component Analysis on power transformed data. **A.** Explained variance per principal component dimension. **B.** Biplot showing the CRFB dataset plotted by the first and second principal component (PC) scores as well as the eigenvectors for each feature dimension shown in the red lines. **C** and **D.** Principal component 1 and 2 eigenvector weights respectively, showing the contributions of each feature in the rotated coordinate axes.

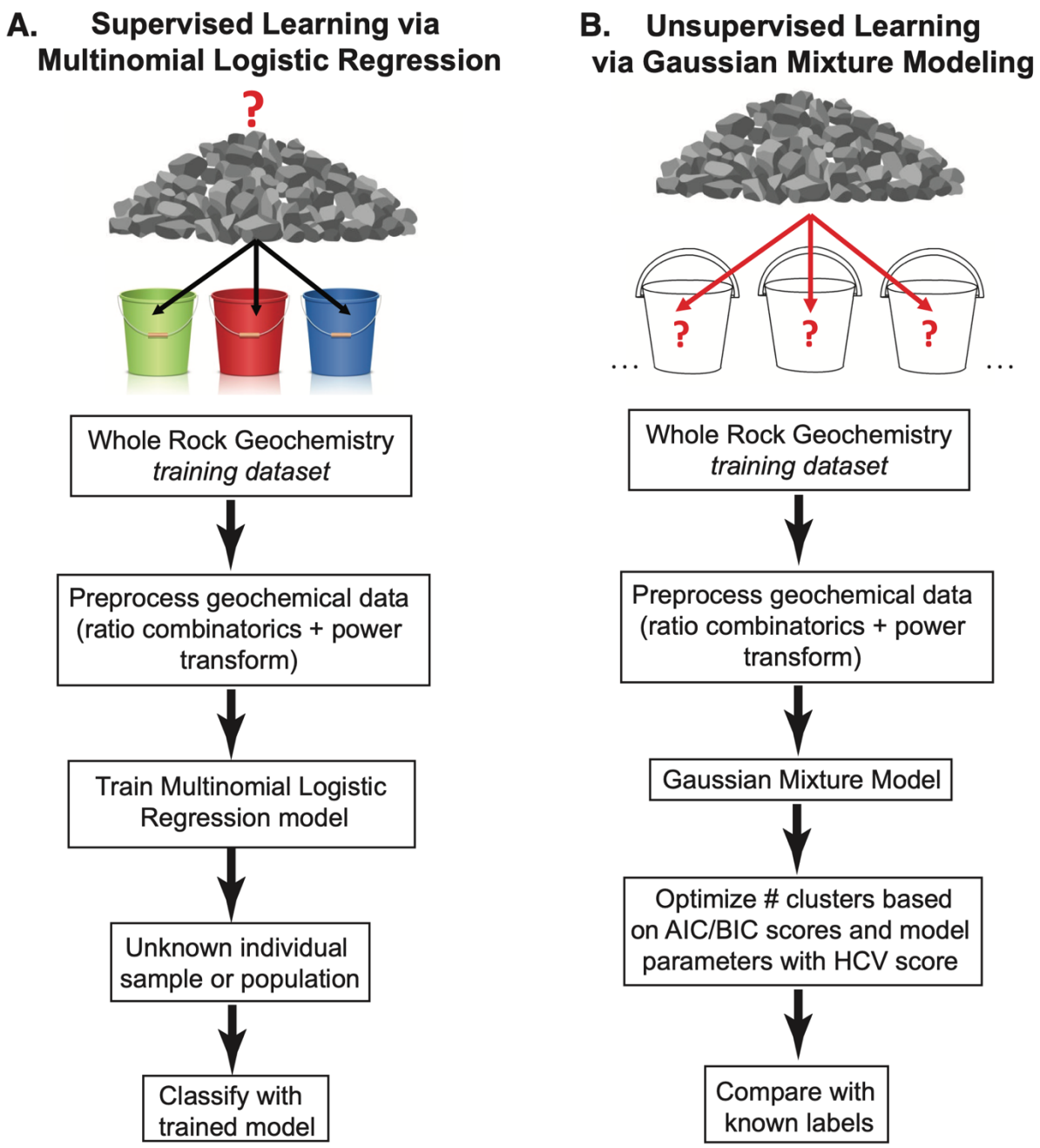

Figure 6: Workflow for **A.** Supervised learning via Multinomial Logistic Regression and **B.** Unsupervised learning with Gaussian Mixture Modeling.

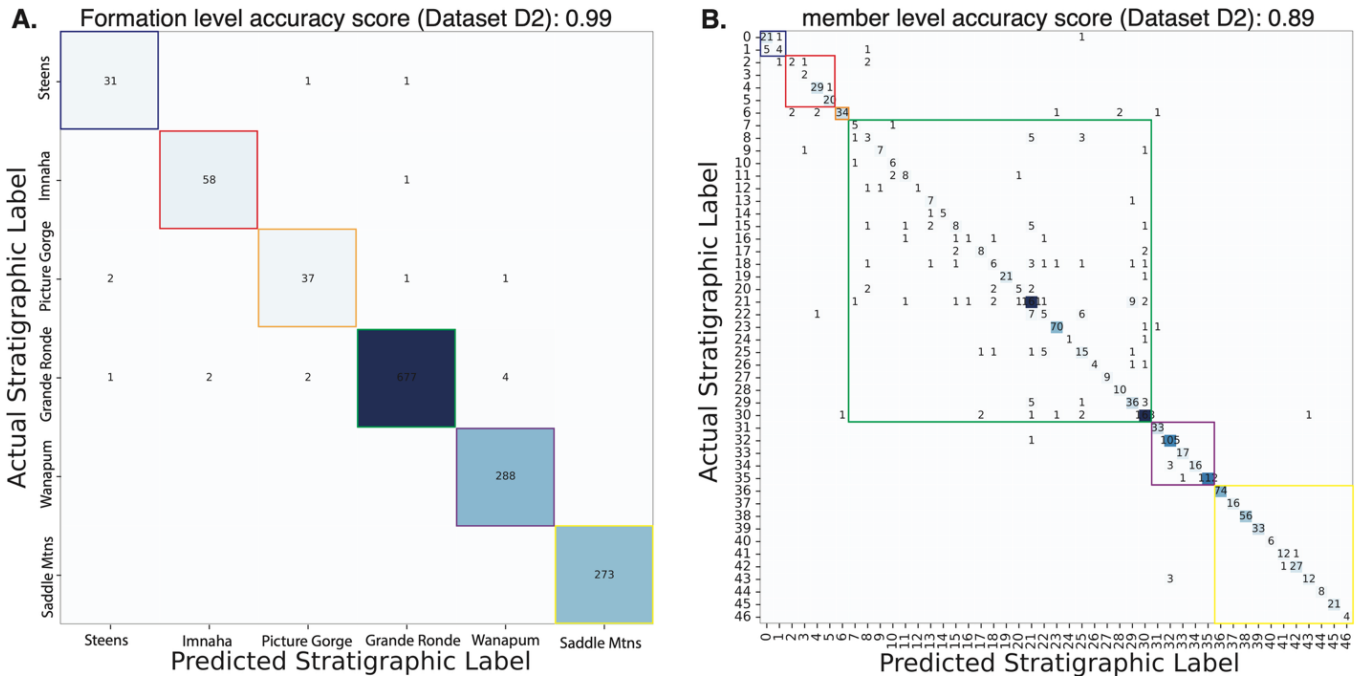

Figure 7: Confusion matrices from the best MLR model associated with the train-test-split approach, using the CRFB D2 data subset. **A.** Formation level (colors match Fig. 1). **B.** Member level, with numbers on the axes that correspond to CRFB members in ascending stratigraphic order as listed in Fig 1.

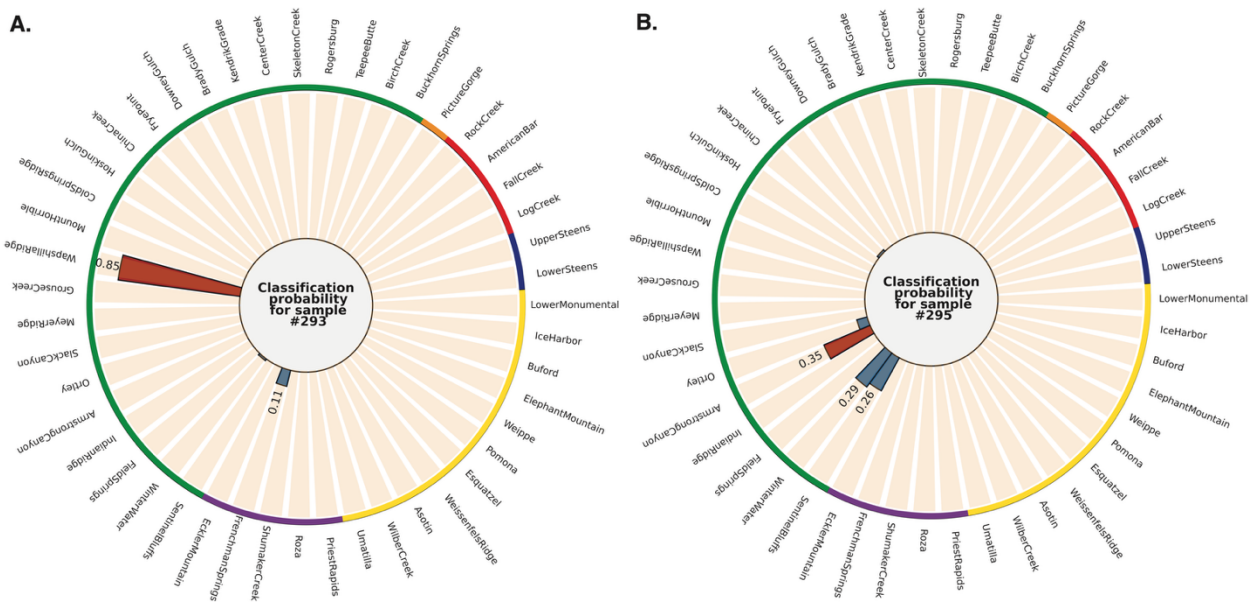

Figure 8: Example circular barplots showing MLR classification probabilities at member level for specific samples in our "undifferentiated" Formation-level CRFB data (Supplemental Dataset S2). **A.)** An example of a clear prediction. **B.)** An example of an ambiguous prediction.

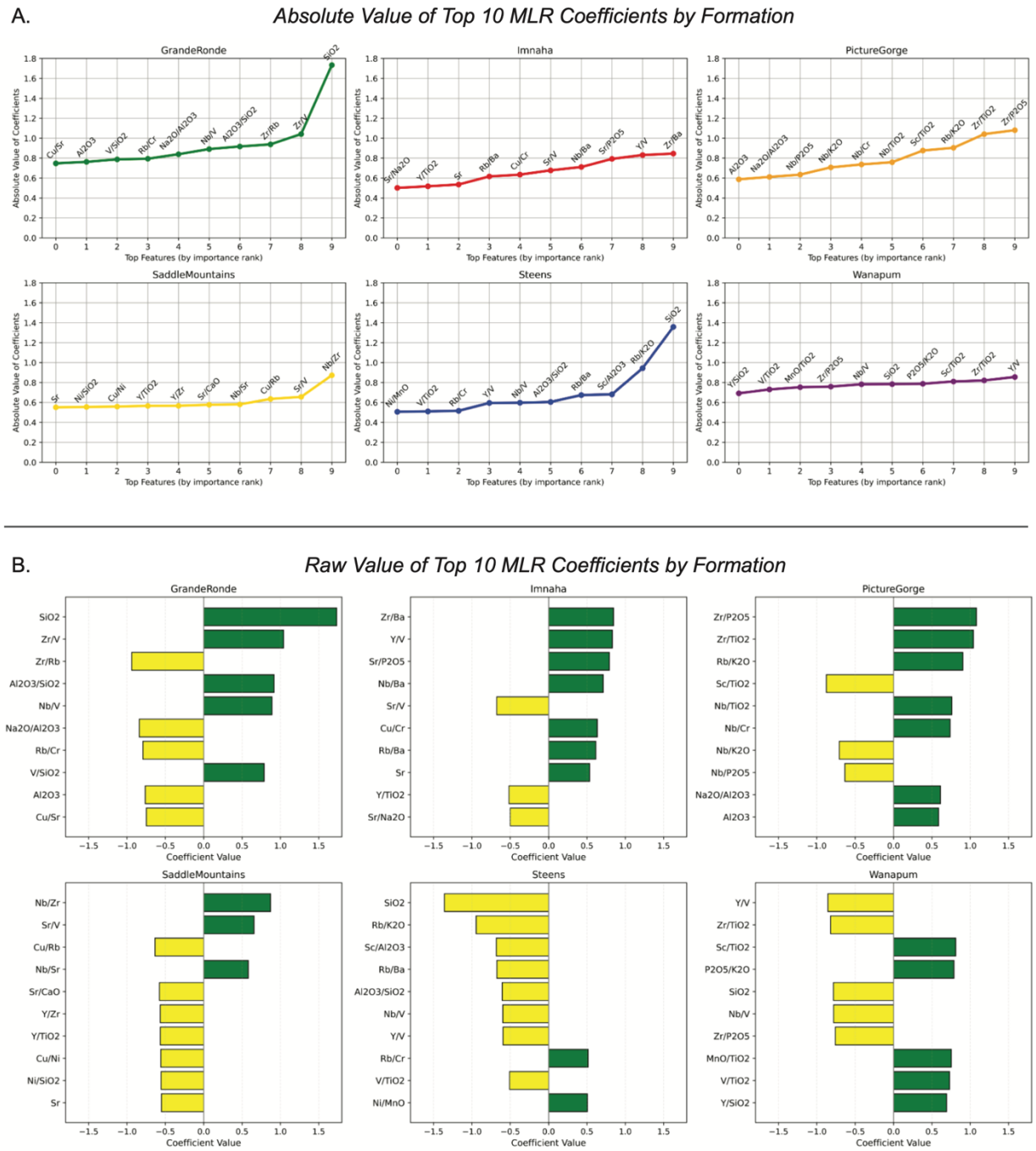

Figure 9: A.) Plots showing the top 10 coefficients for predicting each Formation level class in the CRFB. The y-axis represents the normalized coefficients that the supervised multinomial logistic regression model utilized to create decision boundaries for each class in the dataset on each feature utilized by the model. **B.)** Un-normalized coefficients associated with panel A.

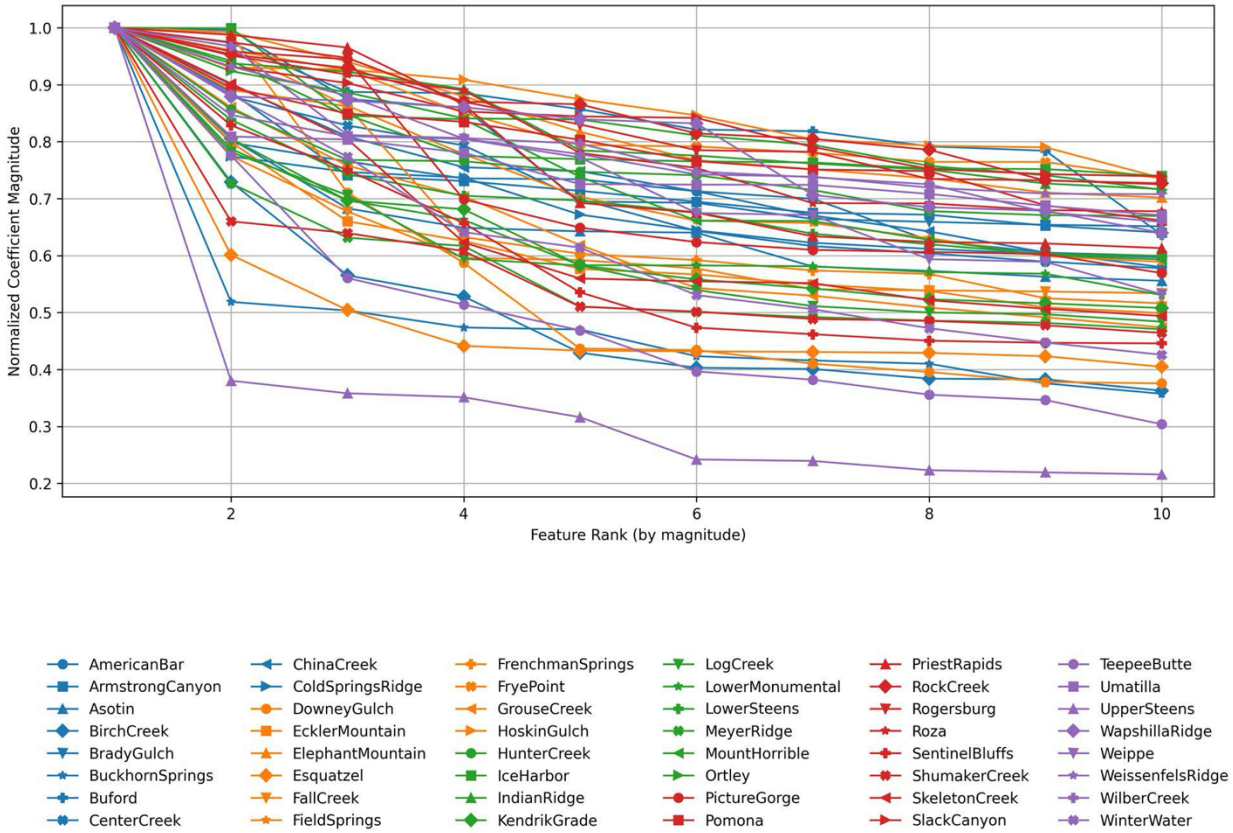

Figure 10: Normalized coefficient magnitude amongst the top 10 ranked features for each member level class in the MLR model for data subset D2. Distributions with steeper slopes across the top 10 ranked require fewer features for model classification.

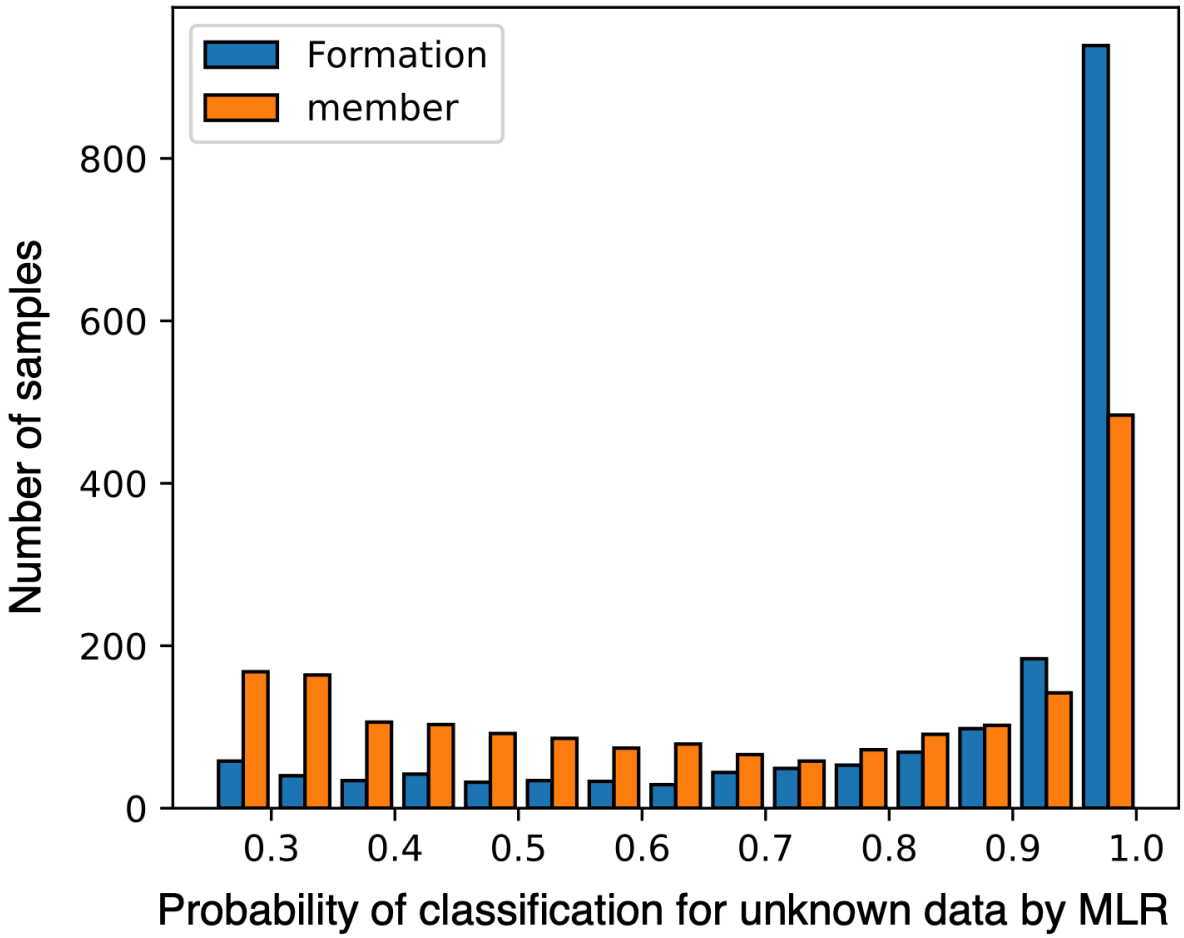

Figure 11: Histograms of MLR classification probability for the unknown CRFB lava dataset (N=1,572), at both Formation and member level using the trained model from data subset D2.

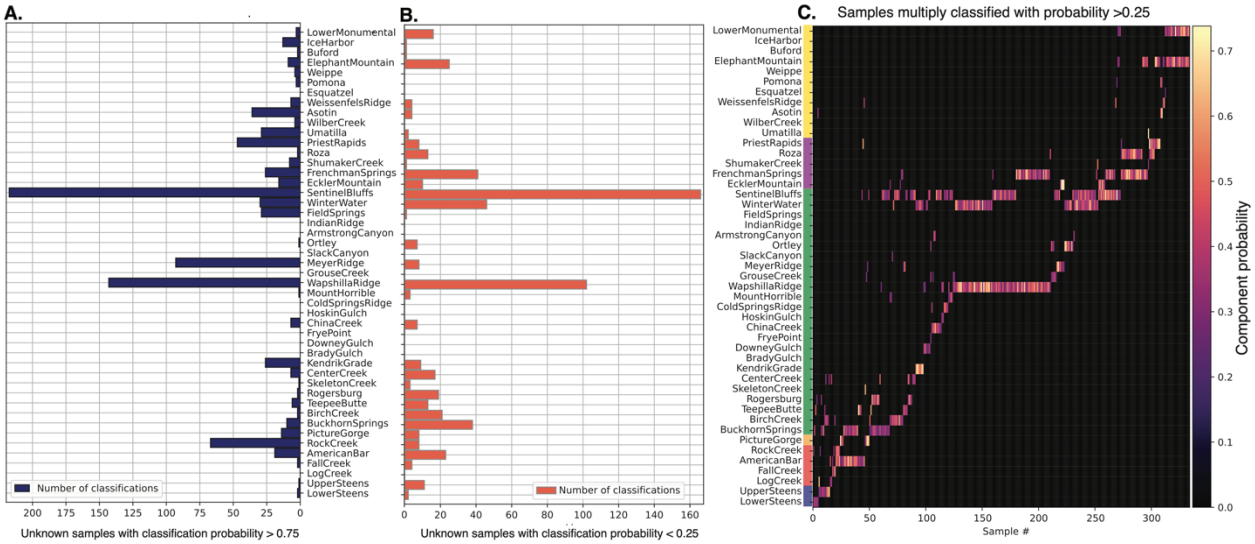

Figure 12: A. Distribution of unknown CRFB lava samples classified at member level by the MLR model at >75% probability. B. Distribution of samples classified at <25% probability. C. Samples classified at >25% probability for two members. Color is the probability of classification on a per-sample basis.

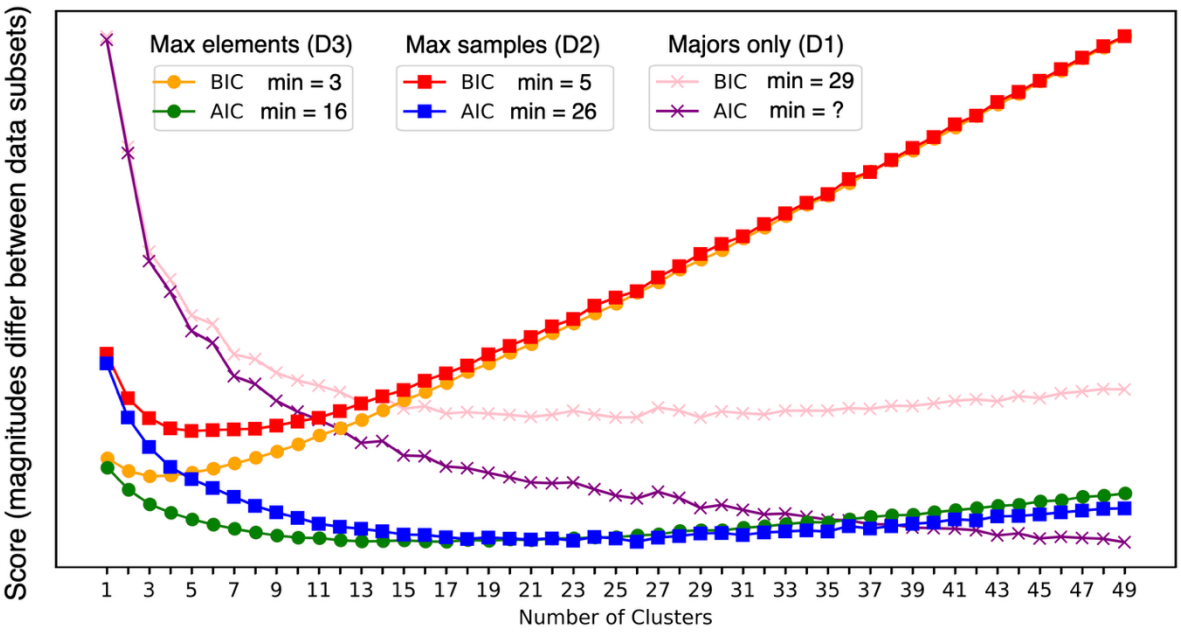

Figure 13: AIC and BIC scores for GMM clustering of each data subset. Y axis units are omitted for the purpose of comparison. All three data subsets are plotted along with the cluster number associated with minimum scores. We focus on GMM of data subset D2 here and specifically study 5 and 21 clusters.

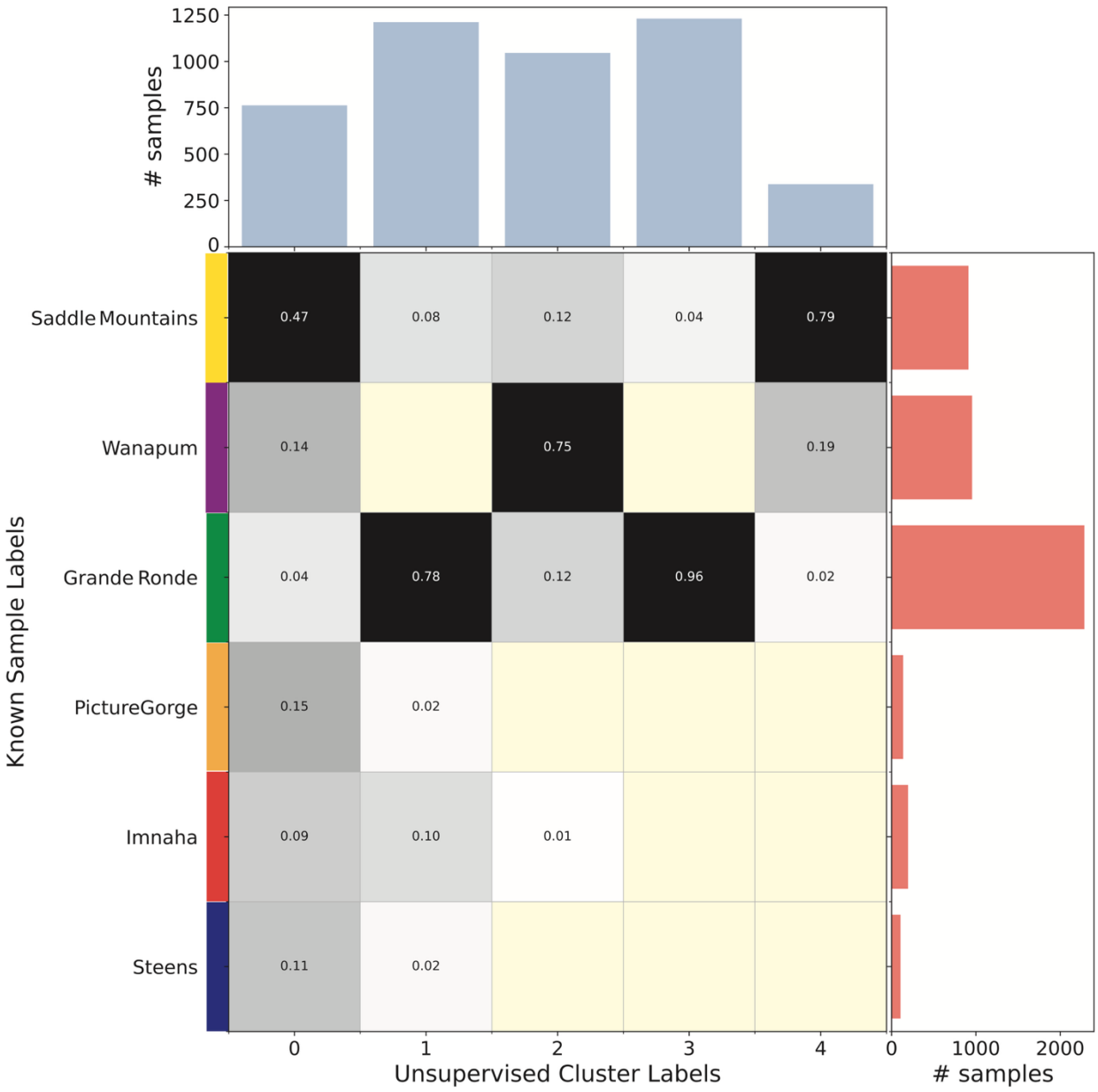

Figure 14: Comparison of GMM cluster assignment groupings (assuming 5 clusters) to known Formation level labels. Colors follow Fig. 1. Boxes with numbers indicate the fraction of a GMM cluster in the corresponding Formation, while yellow boxes contain no samples. Histograms at the top and right indicate the number of samples in each category.

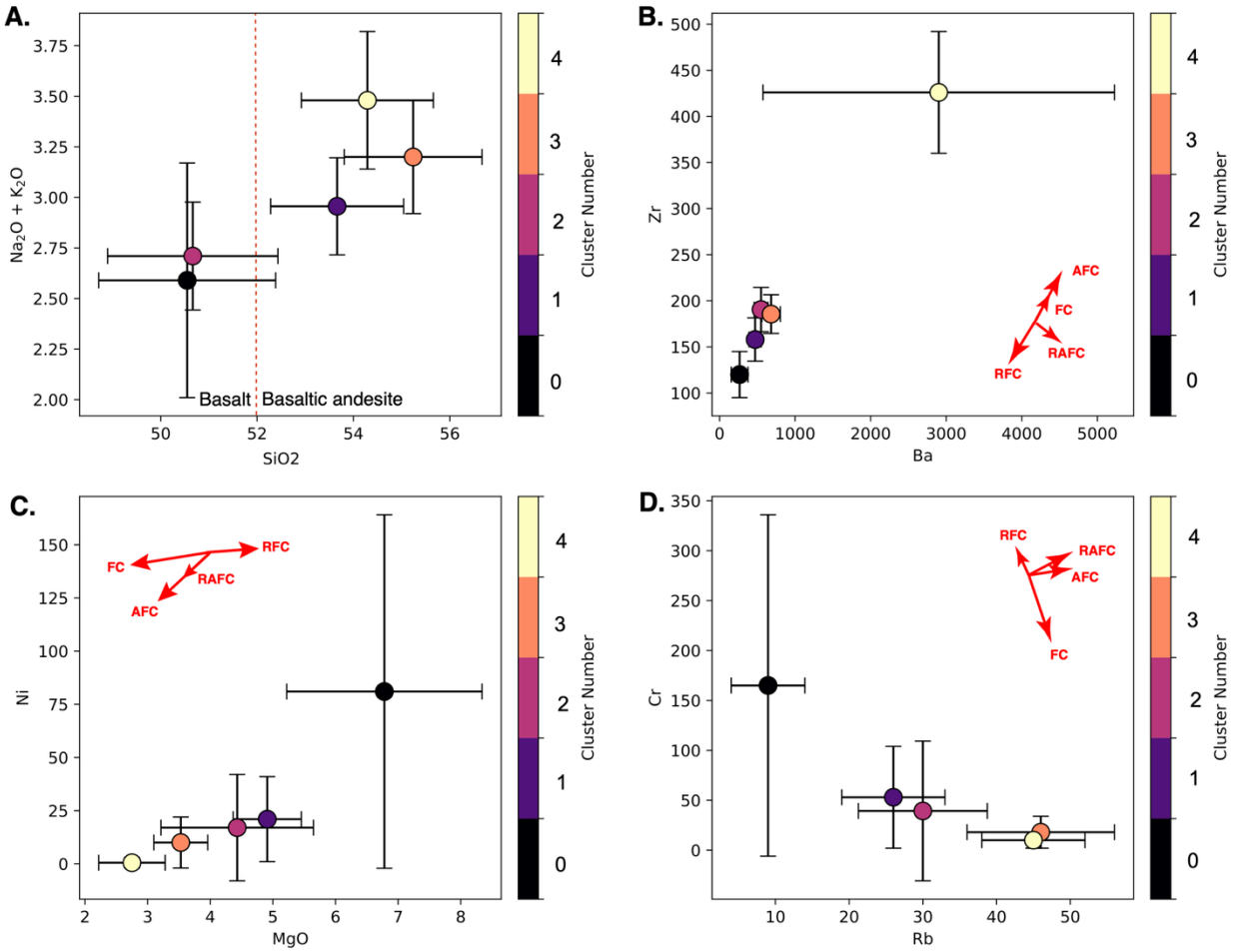

Figure 15: Biplots of GMM cluster centers using data subset D2 with 5 clusters. Points represent cluster median values and error bars are the IQR calculated for the geochemistry of each cluster distribution. Color corresponds to the cluster number in Fig. 14. Red arrows indicate the direction of RAFC based on petrologic modeling (Supplementary Information Section S2).

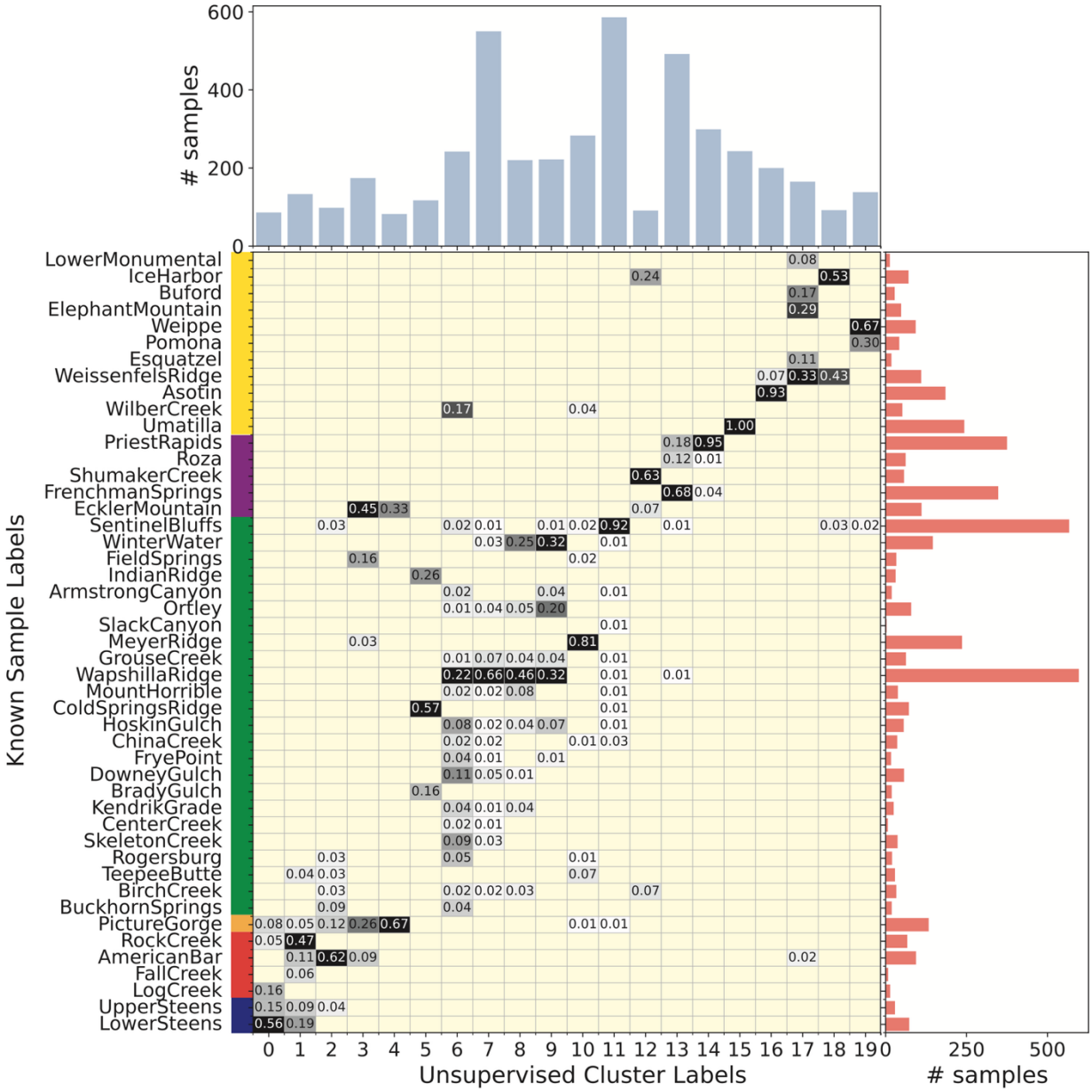

Figure 16: Comparison of GMM cluster assignment groupings (assuming 21 clusters, one empty cluster omitted here) to known member level labels. Formation colors follow Fig. 1 for reference. Boxes with numbers indicate the fraction of a GMM cluster in the corresponding member, while yellow boxes contain no samples. Histograms at the top and right indicate the number of samples in each category.

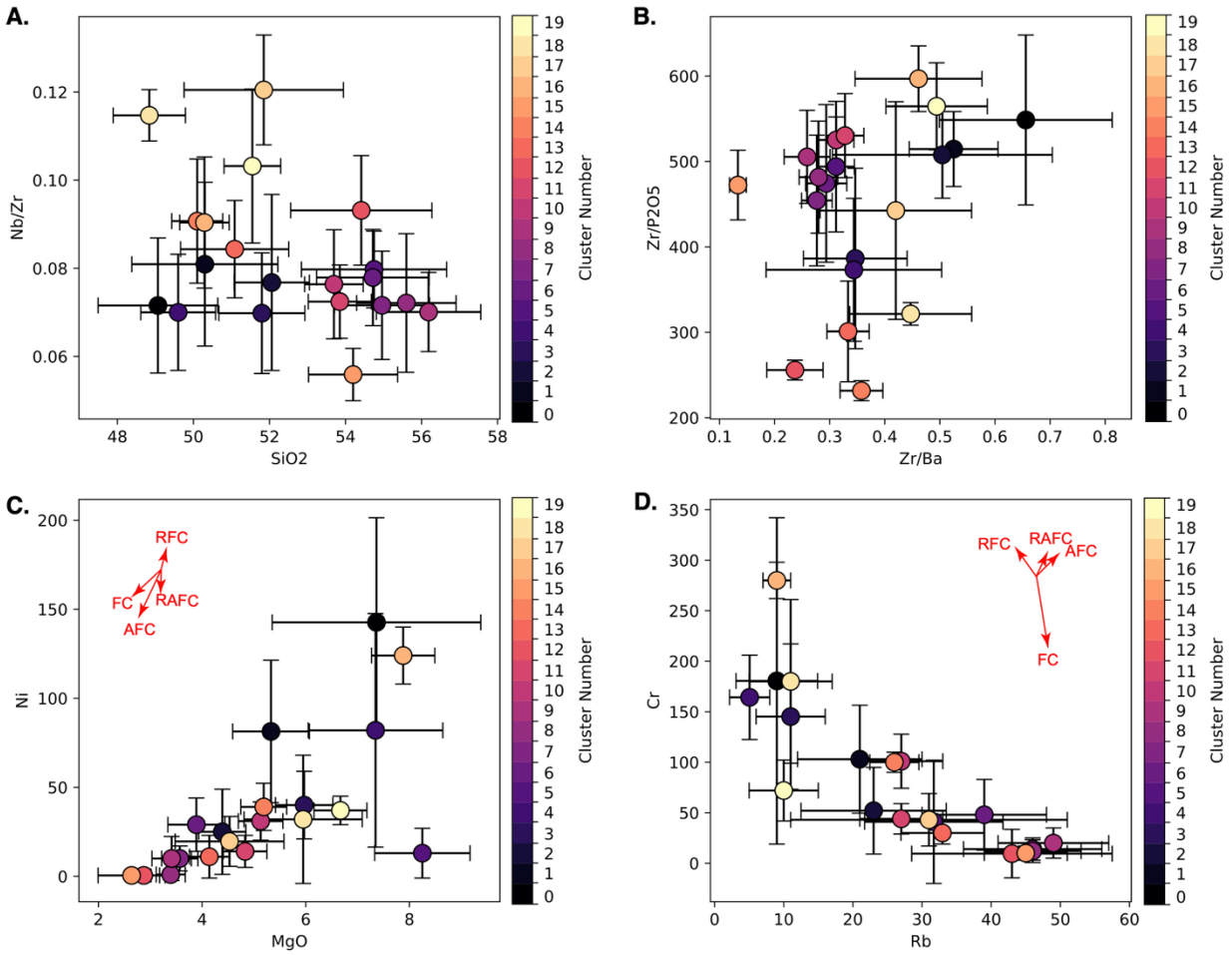

Figure 17: Biplots of GMM cluster centers using data subset D2 with 20 clusters. Points represent cluster median values and error bars represent the IQR calculated for the geochemistry of each cluster distribution. Color corresponds to cluster number in Fig. 16. Additional biplots may be found in Supplementary Fig. S3. Red arrows indicate direction of RAFC based on petrologic modeling (Supplementary Information Section S2).

Supplementary Material

S1. Columbia River Flood Basalt lava data sources

Supplementary Data File S1 is a labeled (at Formation and member level) database of CRFB whole rock geochemistry for Machine Learning model training. In this section we describe this compiled dataset. The separate Supplementary Data File S2 file contains samples for which Formation level labels are available but not member labels. Several existing published datasets are the starting point for any CRB geochemical investigation. Peter Hooper published a seminal dataset that established the full Formation and member level identification of most of the CRB lavas (Wright et al., 1973; Reidel, 1982; Hooper, 2000; Camp et al., 2013; Conrey et al., 2013; Reidel et al., 2013; Reidel, 2015).

In addition to these published datasets, we have incorporated unpublished data from Dr. Steve Reidel and the Washington State Geoanalytical Lab, led by Dr. John Wolff, so that every assumed member in our stratigraphy had sufficient samples to justify training for our Multinomial Logistic Regression model. The analytical lab provided us with 3,600 samples with full major and trace element analyses. In total our database includes 36 sources (see "Reference" column of Supplementary Data File S1).

We also added data from the USGS and OWRD (Oregon Well Resource Department) groundwater well sites in the region available respectively at the USGS website for the Columbia River Basalt Stratigraphy in the Pacific Northwest (Conlon, 2020a) and at the Oregon Water Resources Department's GRID Website ("Oregon Water Resources Department - Well log query tool"). As the holes were drilled, cuttings and core from the holes allowed researchers to collect geochemical information from the lavas that made up the well stratigraphies (Conlon, 2020c). It is worth noting that the USGS stratigraphic nomenclature for the CRFB system (Conlon, 2020b) differs slightly from ours. This is an example of the persistent ambiguity in the stratigraphy today that could be addressed in an objective manner via machine learning (ML) classification.

S1.1 Steens Basalt and Picture Gorge

The larger datasets had some small amounts of undifferentiated Steens data (Hooper, 2000; Wolff et al., 2008; Reidel et al., 2013) but data from the Steens Formation was minimal. Most data for the Steens basalt comes from the work of Dr. Nikki Moore who characterized the

chemical composition of the exposed lava flows in detail (Moore et al., 2018, 2020). Camp et al. (2013) measured and sampled from several stratigraphic sections around Steens Mtn. to characterize the flows; data from this work has been digitized from the published work and added into the larger dataset (Camp et al., 2013). We also include more recent analyses of Upper Steens rocks (Day et al., 2021) as well as a small package of data from an older study on the Steens (Gunn and Watkins, 1970).

Some picture gorge information was available from Dr. John Wolff and the Washington State Geoanalytical Lab, but most of the data we have from this formation came from the work of Dr. Emily Cahoon and collaborators (Cahoon, 2020; Cahoon et al., 2020, 2021, 2023).

S1.2 Imnaha, Grande Ronde, and Wanapum Basalts

The multi-member datasets provide detailed information for the members within the main phase of the CRB, but several small-scale datasets supplemented our geochemical compilation. The work of (Conrey et al., 2013) detailed the geochemistry of three large volume flows of the main phase CRB (Conrey et al., 2013). 1,057 samples taken from various members in the Wanapum and Grande Ronde formations were compiled from a study by Yuh et al. in 2022 (Yuh et al., 2022). A small sample batch was also added from the work of Drs. Cruz and Streck (Webb et al., 2019; Cruz and Streck, 2022). This data has been included in the compilation and was collected from the Littlefield area (Cruz and Streck, 2022). These basalts were collected in conjunction with study of the Dinner Creek Tuff which fell within the lava stratigraphy in the area (Webb et al., 2019; Cruz and Streck, 2022). Additional Imnaha Formation geochemical data was added from a 2023 study on the earliest CRFB magmas (Streck et al., 2023) and additional Grande Ronde data across formations was provided by Dr. Stephen Reidel in 2022 to fill in the gaps in member data.

Variation within distinct flows that have been identified within the Sentinel Bluffs member has generated debate (Reidel, 1982, 2005; Reidel and Tolan, 1989; Sawlan, 2017, 2019; Baker et al., 2019) about the stratigraphy of this flow. Sawlan (2017) used geochemical variation in Mg and other elements to identify a signature of alteration within this flow (Sawlan, 2017). As a result, we have been able to accumulate 766 samples of this member.

Work west of the Cascade mountains through the Columbia River Gorge also increased the amount of data coverage for some main phase members. We used data from the Wells et al., (2009) Field Trip Guide which compiled data on the CRB group from the Cascade Range to the Pacific Ocean (Wells et al., 2009). Additional data was added from mapping collections. 308 samples of main phase CRB was collected during mapping of the Greater Portland Metropolitan Area and Surrounding Region by Wells and colleagues and published (Wells et al., 2009, 2020). 60 more samples were added from three Map Quads compiled by USGS researcher Dr. Russ Evarts primarily: the Geologic Map of the Washougal Quadrangle, Clark County, Washington, and Multnomah County, Oregon (Evarts et al., 2013), the Geologic Map of the Woodland Quadrangle, Clark and Cowlitz Counties, Washington (Evarts, 2004b) and the Geologic Map of the Saint Helens Quadrangle, Columbia County, Oregon, and Clark and Cowlitz Counties, Washington (Evarts, 2004a).

Careful attention was paid specifically to gathering data for the Wapshilla Ridge flow (presumed to be the largest volume flow in the CRFB stratigraphy). There were many contributing sources to this compilation of Wapshilla Ridge data, including both academic papers and government reports from Oregon, Washington, and Idaho and geologic maps (Reidel et al., 1992; Schuster, 1993; Ferns, 1999, 2002; Ferns and Madin, 1999; Derkey et al., 1999, 2004; Bush et al., 2001, 2004, 2005, 2018; Madin, 2004; Caprarelli and Reidel, 2004; Ferns and McConnell, 2005, 2015; Garwood and Bush, 2005; Schmidt et al., 2005, 2009; Derkey and Hamilton, 2007; Garwood et al., 2008; Kauffman et al., 2008, 2011; Madin and Niewendorp, 2008; Dinterman and Duvall, 2009; Reidel and Tolan, 2013; Evarts and Fleck, 2017; U.S. Geological Survey, 2019; EarthRef.org, 2019). Additional data was provided by Dr. Stephen Reidel via personal communication in 2019, who generously provided us with data on geochemical sections through the Wapshilla Ridge member.

S1.3 Saddle Mountains

The compiled dataset contains 1,450 Saddle Mountains geochemical samples. These come primarily from the compilation work of John Wolff and the Washington State Geoanalytical Lab (Hooper, 2000; Reidel and Tolan, 2013), and the work of Dr. Peter Hooper (2000) and Dr. Steve Reidel (2013). Dr. Don Swanson's data compilation of Wanapum and Saddle Mountains samples also helped to provide more data for this formation (Swanson et al.,

1989). Additional data from the OWRD and USGS well databases supplemented these composite datasets.

S2: Modeling petrologic evolution with the Magma Chamber Simulator

To assess the potential roles of RAFC processes (Fig. 15 and 17 in the main text), we perform calculations of idealized magmatic differentiation scenarios using a thermodynamic model, the Magma Chamber Simulator (Bohrson and Spera, 2001; Bohrson et al., 2014). The Magma Chamber Simulator (MCS) predicts equilibrium compositions (major and trace elements) under variation of thermodynamic parameters in a magmatic system (Bohrson et al., 2014). The MCS is based on the MELTs thermodynamic calculator (e.g., (Ghiorso and Sack, 1995), combining the MELTs minimization of Gibbs free energy with an enthalpy balance to understand the effect of assimilation and recharge on the equilibrium phase relations of magma (Bohrson and Spera, 2001; Bohrson et al., 2014).

MCS simulations are conducted as follows: we model intrusion of a parental basalt composition, matching average Imnaha basalt composition (calculated as an average of values in our database), into batholithic crust (Fig. S1, S2). This magma is intruded at 5 kbar pressure into a defined country rock composition with a mass ratio of 2:1 wall rock to basalt. In each scenario the magma is instantaneously emplaced into the crust and begins a temperature descent in increments of 20°C starting at 1400°C. Heat transferred to the wallrock drives partially melt once it reaches the solidus temperature. In each simulation the partial melt is assimilated (homogenized) into the remaining melt once it reaches a melt fraction of 0.05. The simulation ends when the magma and wallrock reach the same temperature or once the magma reaches 850°C, whichever comes first. During model runs that incorporate recharge, as the temperature of the melt drops to a certain temperature (in this case 1100°C), magma with composition equivalent to the Imnaha parent was added to the melt in a proportion of 50% by mass. While assimilation and fractional crystallization occur gradually over many time steps, recharge is a short-lived process that imparts an immediate but short-lived signal (unlike a real system where recharge may be more sustained). Once the recharging magma is added to the chamber it is immediately considered well mixed and begins to undergo AFC processes once again, from a more primitive composition than the previous steps. Other isobaric pressure scenarios (from 2-10 kbar) can be found in (Hampton, 2022).

We model four wallrock compositions in the mid crust (5 kbar): An average mid continental crust (granodiorite) (Rudnick and Gao, 2003), an average upper continental crust (granite) (Rudnick and Gao, 2003), the unmelted composition of tonalite from the Wallowa Mtns. (Petcovic and Dufek, 2005), and the average composition of the Atlantic pluton within the Idaho Batholith (Gaschnig et al., 2011) (Fig. S1). We also study the potential influence from recharging mafic magma similar in composition to the Imnaha (e.g., Wolff and Ramos, 2013). We calculate the percent change for each element in the magma melt during various permutations o Recharge, Assimilation and Fractional Crystallization, (RAFC) (Bohrson et al., 2014), shown in Fig. S2.

The effect of the different wallrock assimilant compositions is particularly evident when we plot the composition of partial melt from each wallrock melting scenario (Fig. S1). The partial melt consists in all cases of enrichments in incompatible elements (Fig. S1). The Idaho Batholith partial melt composition is depleted in Cr, V and Ni versus the other partial melts (Fig. S1, S2). It also has orders of magnitude higher Ba and Rb than Wallowa batholith partial melt or partial melt generated from generalized crustal compositions (Fig. S1). The partial melting of the Wallowa tonalite composition results in a marked enrichment in Zr concentration, but experiences overall less partial melting and less enrichment in other incompatible elements.

In every simulation fractional crystallization causes a strong depletion in Cr and relatively less strong depletions in MgO and CaO when the percent change within each process was calculated (Fig. S2). At the same time, FC increases other more incompatible trace elements, though not to the same degree as the addition of assimilant (Fig. S2). This is consistent with crystallization of clinopyroxene as the primary phase by mass and with secondary crystallization of plagioclase. Secondary crystallization of olivine and orthopyroxene also occurs during simulations.

Assimilation of each type of wallrock increases the trace element concentration of Rb, Ba, Zr, Y, Nb, La, Ce, Nd, and Lu (Fig. S1). However, the strongest signal of trace element increase comes from assimilation of partial melt derived from the Idaho Batholith composition. In this wallrock scenario Rb and Ba particularly experience a strong increase in the magma melt (Fig. S2). The Wallowa batholith also increases the trace element concentrations; however, it most significantly affects Zr and has the lowest effect on Ba and Rb concentration, which are

important sources of variation within the CRFB dataset (e.g., Fig. 15 and 17 in main text). This suggests that at least one likely assimilant may be compositionally close to the Idaho Batholith.

Recharge of Imnaha melt has some distinct effects on the magma melt composition in comparison to FC or AFC (Fig. S2). Many of the incompatible trace element concentrations are decreased while more compatible elements such as Cr and MgO increase in the magma (Fig. S2). However, this is RFC and not just recharge alone. If this RFC was the primary process affecting our melt, we would not expect Cr to dominate the variation. Rather we would expect to see strong trends toward a more primitive magma, for example a decrease in incompatible trace element concentration and trends in MgO.

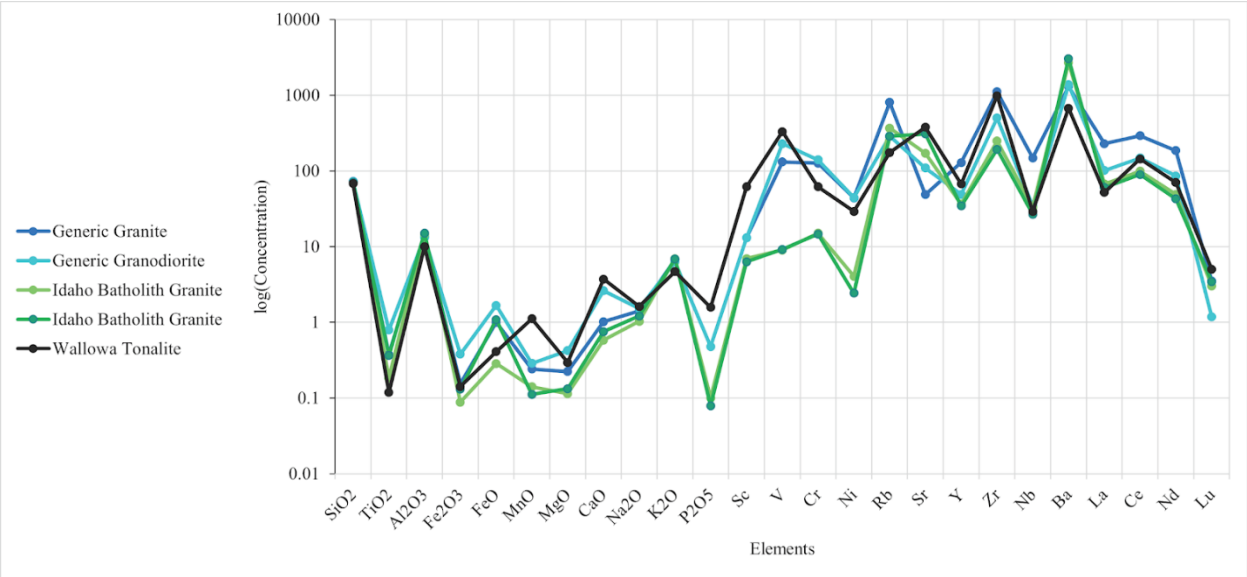

Supplemental Figure S1 *Compositions of partial melt created during various AFC experiments of the Magma Chamber Simulator* (Bohrson et al., 2014)*. The Idaho Batholith is run under two scenarios, one including recharge and one without recharge* (Gaschnig et al., 2011)*, shown in green. This figure presents only the results for the simulation at 5000 bars of pressure, which captured all main processes. In each scenario the magma is instantaneously emplaced into the crust and begins a temperature descent in increments of 20°C starting at 1400°.*

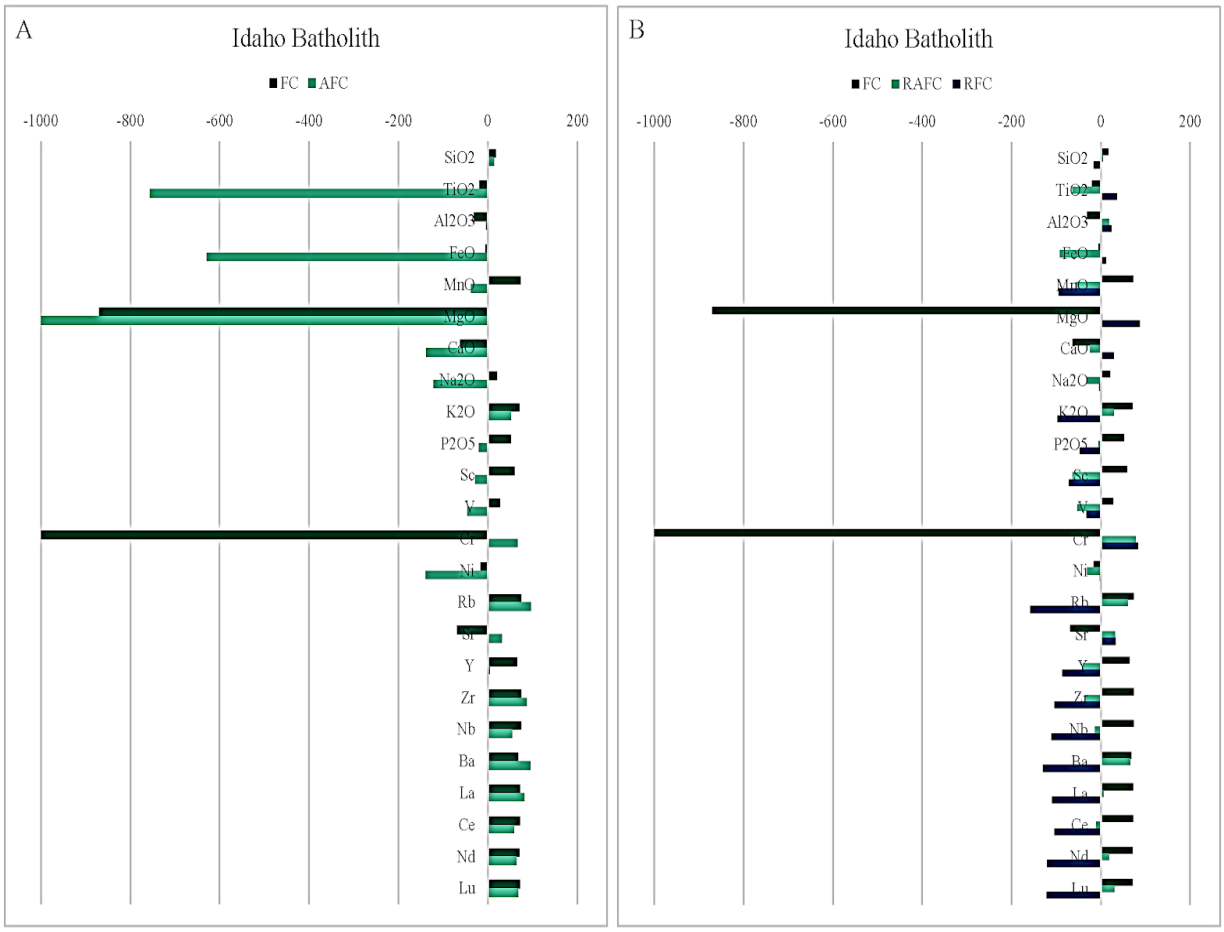

Supplemental Figure S2 *A) The calculated percent change in each element during model runs that isolate various RAFC scenarios from the reported results of the MCS, assuming an initial Imnaha parent composition and Idaho batholith composition assimilant. B) percent change including instances of recharge (RAFC) by an Imnaha composition magma. The top bar in each element is the same as in panel A. This presents results for the pressure temperature conditions of 5000 bars of pressure, where the magma is instantaneously emplaced into the crust and begins a temperature descent in increments of 20°C starting at 1400°.*

S3. Multinomial Logistic Regression model statistics and trained models

Classification level	Data subset	Num Samples	Num Features	Precision	Recall
Formation	D3	4007	276	0.994	0.994
Formation	D2	4600	210	0.989	0.989
Formation	D1	6259	45	0.926	0.926
Member	D3	4007	276	0.913	0.914
Member	D2	4600	210	0.893	0.897
Member	D1	6259	45	0.822	0.831

Table S1. MLR classification statistics for each data subset considered here.

The github repository https://github.com/leifkarlstrom/CRB_ml_classifiers contains MLR models associated with data subsets D1-D3, which are available as .csv files as well as accessible via a python Jupyter notebook Classify_from_trained_CRBmodel.ipynb. This script loads one of these models and uses it to classify samples in the undifferentiated CRB database (Supplementary Dataset S2). Plots similar to those included in the main text are generated. The code used to train new MLR models is also available at this repository.

These trained models can be easily modified to classify any CRFB geochemical data, provided that these data include the elements used.

S3. Additional GMM results

Here we show additional biplots to illustrate other elemental differences between GMM groupings for the 21 cluster case, representing in power-transformed axes. The github repository https://github.com/leifkarlstrom/CRB_ml_classifiers contains scripts to train and plot results from GMM models.

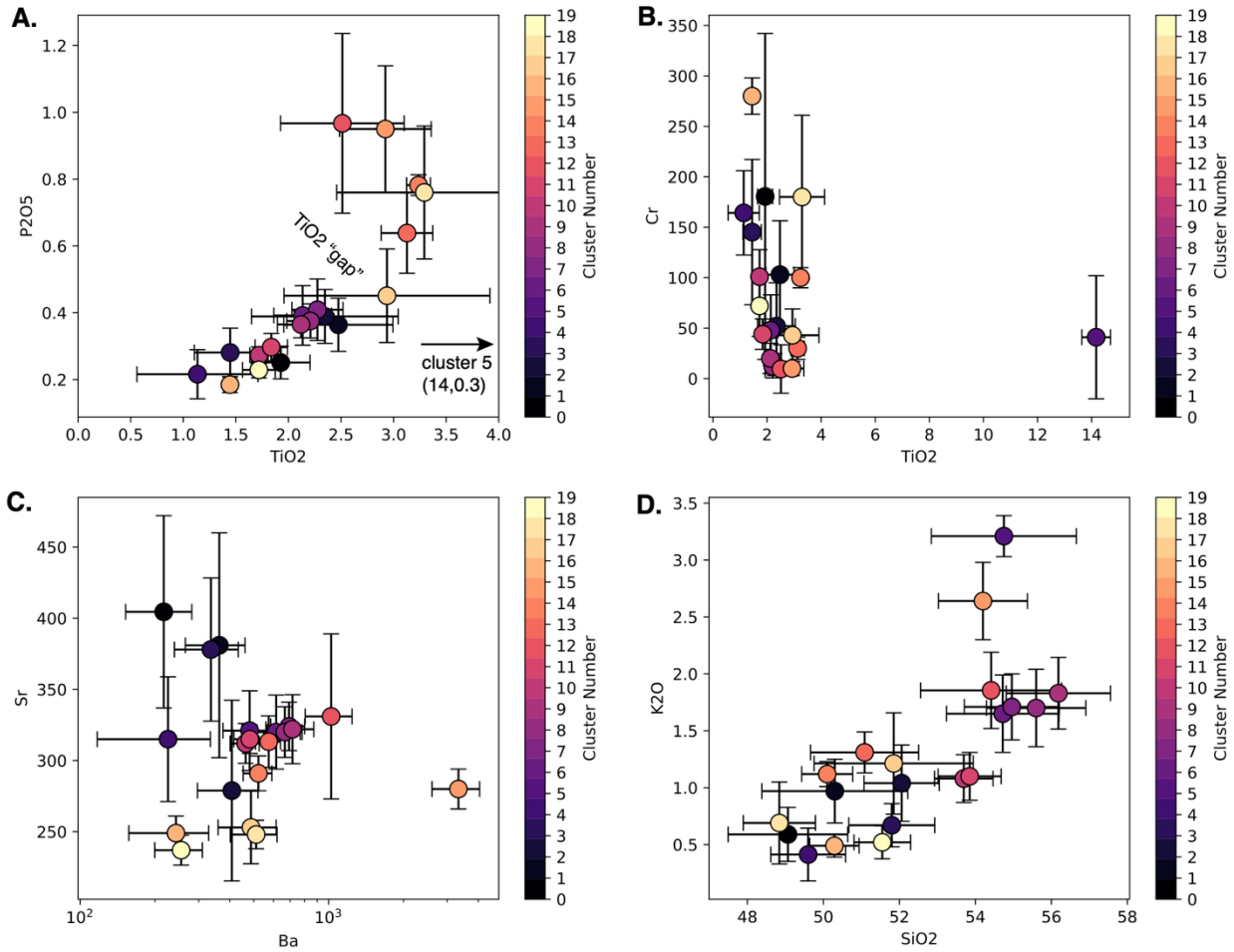

Figure S3. Additional biplots to augment Fig. 17 in the main text. Symbols are cluster medians, while error bars are cluster interquartile range. (A) P_2O_5 versus TiO_2. Note the "Ti gap" articulated by Hooper et al., (2007) separating clusters with dominantly Wanapum membership (cluster numbers are as given in Fig. 16 of main text) from other formations. (B) Cr versus TiO_2. (C) Sr versus Ba, plotted by (Sawlan, 2017) *to track alteration. (D) K_2O versus SiO_2.*

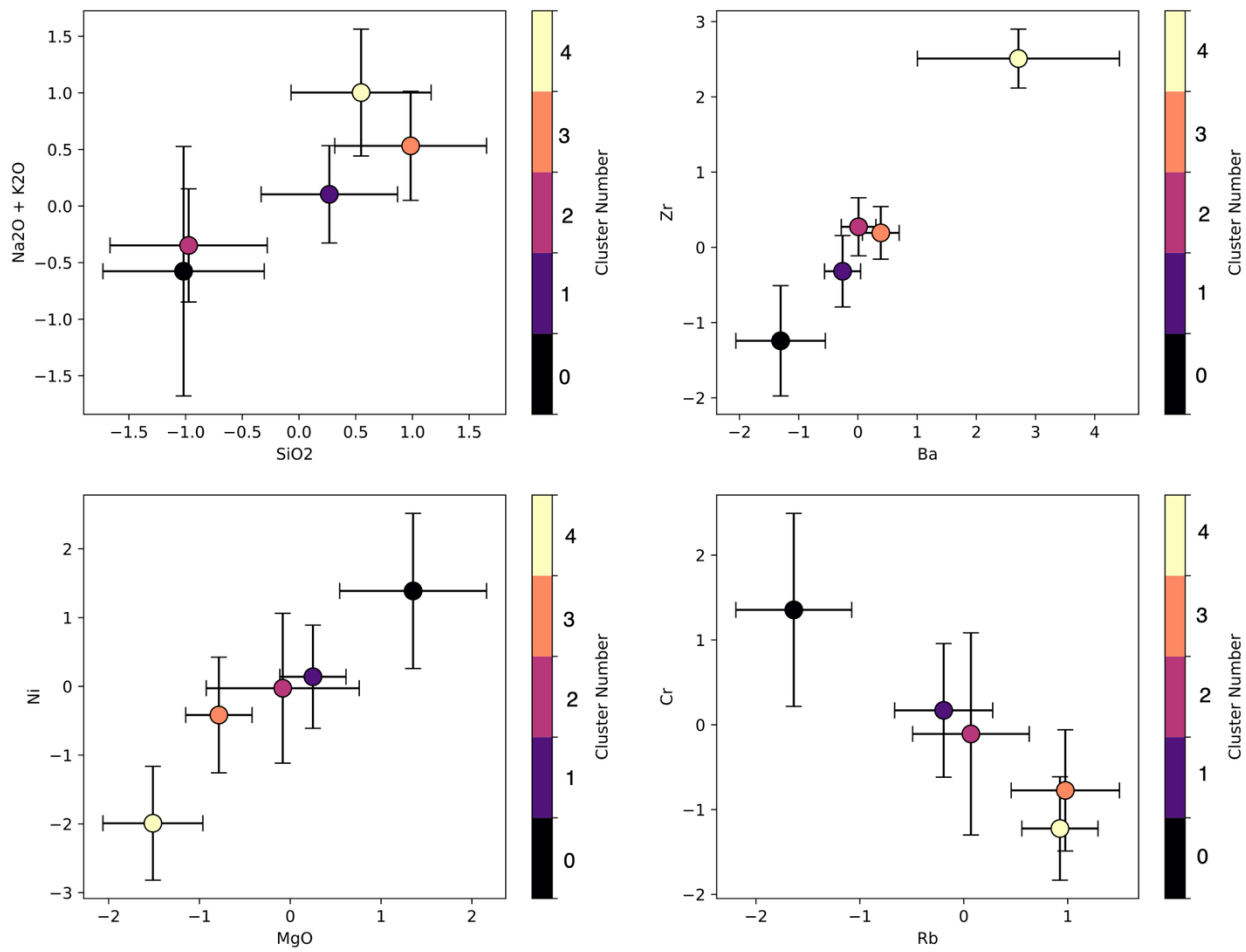

Figure S4. Same as Fig. 15 in the main text but displayed in terms of Power Transformed axes (which is what we use for GMM clustering). Cluster numbers are those in Figure 14 of the main text.

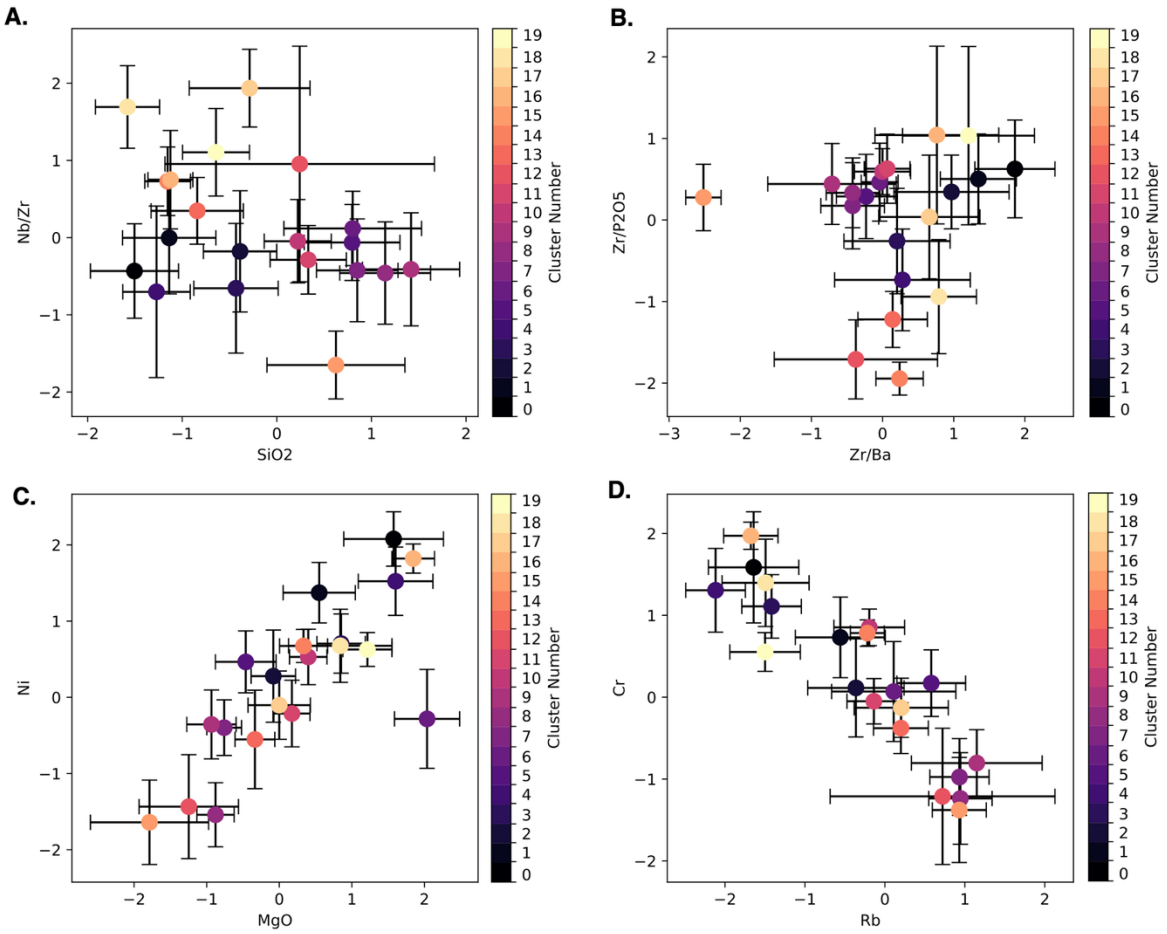

Figure S5. Same as Fig. 17 in the main text but displayed in terms of Power Transformed axes. Cluster numbers are those in Figure 16 of the main text.